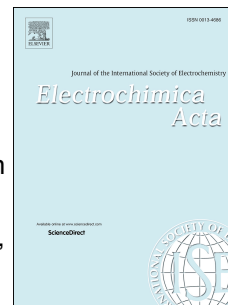# Journal Pre-proof

Kinetic Monte Carlo applied to the electrochemical study of the Li-ion graphite system

E.M. Gavilán-Arriazu, O.A. Pinto, B.A. López de Mishima, D.E. Barraco, O.A. Oviedo, E.P.M. Leiva

Please cite this article as: E.M. Gavilán-Arriazu, O.A. Pinto, B.A. López de Mishima, D.E. Barraco, O.A. Oviedo, E.P.M. Leiva, Kinetic Monte Carlo applied to the electrochemical study of the Li-ion graphite system, *Electrochimica Acta* (2020), doi: https://doi.org/10.1016/j.electacta.2019.135439.

This is a PDF file of an article that has undergone enhancements after acceptance, such as the addition of a cover page and metadata, and formatting for readability, but it is not yet the definitive version of record. This version will undergo additional copyediting, typesetting and review before it is published in its final form, but we are providing this version to give early visibility of the article. Please note that, during the production process, errors may be discovered which could affect the content, and all legal disclaimers that apply to the journal pertain.

Kinetic Monte Carlo applied to the electrochemical study of the Li-ion Graphite System

E.M. Gavilán-Arriazu[1,2], O.A. Pinto[2], B.A. López de Mishima[2], D.E. Barraco[3], O.A. Oviedo[1], E.P.M Leiva[1]

[1]Departamento de Química Teórica y Computacional, Facultad de Ciencias Químicas, Universidad Nacional de Córdoba, INFIQC, Córdoba, Argentina.

[2]Instituto de Bionanotecnología del NOA (INBIONATEC). Universidad Nacional de Santiago del Estero (UNSE); CONICET. RN 9, Km 1125. G4206XCP, Santiago del Estero, Argentina.

[3]Facultad de Matemática, Astronomía y Física, IFEG-CONICET, Universidad Nacional de Córdoba, Córdoba, Argentina

maxigavilan@hotmail.com, eze_leiva@yahoo.com.ar

Abstract

To delve deeper into the kinetics involved in the staging phenomena of lithium insertion into graphite, it is necessary to develop theoretical models that emulate the physical phenomenon involved. In the present work kinetic Monte Carlo simulations are used to carry out a thorough analysis of the Li-ion graphite system, with the twofold aim of providing atomistic support for interpretations based on several experimental electrochemical techniques commonly used in the laboratory and of making theoretical predictions for future experimental work. Cyclic voltammograms and chronoamperometric transients are obtained, and diffusion coefficients and exchange current densities are calculated at different Li loadings of graphite. These results are compared with selected experimental data from the literature. In this way, there emerge details that cannot be observed in ordinary experiments due to methodological/instrumental limitations. For example, it is found that chronoamperometric responses are different for intercalation and deintercalation, the latter being a faster process. The reason why these phenomena are different is revealed, supporting and widening experimental assumptions. The present results also suggest that

the intrinsic hysteresis observed in experimental work (and in simulations) is due to kinetic factors.

1. Introduction

The graphite anode, of widespread use in commercial Li-ion batteries, has been extensively researched since the 1970's [1,2] and experimental electrochemical techniques have been an important tool to understand and characterize its properties. Due to instrumental and methodological limitations, however, there are still some gaps in the knowledge of this system. One of the most critical restrictions stems from the fact that the system cannot be directly analyzed in atomistic detail. Consequently, there remain some uncertainties in the interpretation of experimental electrochemical results.

The works of Dahn [3] and Ohzuku et al. [4] were seminal in connecting the electrochemical behavior of lithium-graphite intercalation compounds (LGIC) with their x-ray diffraction response. These authors prepared electrodes with different Li-ion loadings and recorded the corresponding x-ray patterns, with the finding of several structures that are called stages. They identified a number of nth-stage compounds, where this denomination corresponds to the formation of Li^+ intercalant layers arranged between every n graphite layers. This work provided the background to interpret research work done employing electrochemical techniques, which were applied to delve deeper into other aspects of this paradigmatic system. In this line, Levi et al. [5] developed a series of articles using cyclic voltammetry at different sweep rates to analyze temperature impact [6] and system size [7] on the Li-ion/graphite system. These authors observed variations in the width, current peak height, and potential peaks separation in the different cases analyzed. Depending on the potential sweep rate, the analysis yielded two different behaviors for thin electrodes: at slow sweep rates the magnitude of the current peak was found to change linearly with the sweep rate, while at fast sweep rates the peak current

presented a linear relationship with the square root of the sweep rate, suggesting semi-infinite diffusion control [5].

While cyclic voltammetry is useful to get a first-sight view of the energy landscape of the system, other techniques were found more effective to delve deeper into the processes involved in lithium insertion/deinsertion phenomena. This is the case of potential-step chronoamperometric experiments, which lead into the kinetics of Li-ion insertion and deinsertion in graphite, analyzing the response of current i with time t [8]. Levi et al. [9] carried out a series of chronoamperometric experiments in lithium-ion graphite systems. These authors sought to understand the shape of the chronoamperometric curves obtained when the system is made of a single phase or two different phases, using potential step techniques. Based on the literature work (ref [10]), they argued that a parameter denoted as Λ , which characterizes the relative contributions of diffusion, kinetic and ohmic resistances, is the key factor to understand the current response. Different ways of representing i vs. t were applied. In the case of potential steps where the system remains at the same stage (for example stage Id in LGIC), they observed a single peak with a maximum in the $it^{1/2} vs \log t$ representation, which is due to slow ion exchange at the interphase and/or to large ohmic drop (small Λ). In the case of potential steps where there is a change from a stage to another, the $it^{1/2} vs \log t$ plot presented two peaks. The authors stated that the occurrence of two peaks can be explained by two different behaviors: at the beginning of the insertion process (for example), when only a few particles enter the system, and there is still only one stage formed, the current is controlled by charge transfer and ohmic drop. After the second stage is formed, as ion concentration increases, the current response changes because diffusion control becomes more important (Λ rises). In this way the process is now controlled by charge transfer/ohmic drop and diffusion. By analyzing the current response with time and $it^{1/2} vs \log t$, Levi et al. [11] also noted differences between the Li-ion intercalation and deintercalation phenomena in graphite. They proposed that this is due to the nucleation and growth of the stage with a higher amount of Li in the intercalation case, and they

highlighted that this may be the reason why they observed that deintercalation is faster as compared with intercalation.

Diffusion of lithium ions inserted in graphite has been a topic of discussion through the years, since different diffusion coefficients have been obtained with various experimental techniques. Nuclear magnetic resonance (NMR) [12], electrochemical impedance spectroscopy (EIS) [13], AC impedance [14] potentiostatic intermittent titration technique (PITT) and galvanostatic intermittent titration technique (GITT) [15], cyclic voltammetry (CV) [16], study of the ratio of potentio-charge capacity to galvano-charge capacity (RPG) [17] were some of the techniques used. In particular, Levi and Aurbach [15] have compared diffusion coefficients (D) obtained through different techniques (EIS and PITT). To illustrate the behavior of D for different occupations of the graphite lattice, say x, these authors have presented plots of $\log(D)$ vs. x (Fig 5, 6, and 7 of [15]), where diffusion coefficients were obtained not only for different lithiation stages but also for intermediate arrangements of x . There are a few simulations works regarding this topic. Lehnert et al. [18] have studied lithium diffusion in graphite using Monte Carlo simulations based on Hartree-Fock calculations. Persson et al. have calculated the diffusion coefficients for stages I and II [19] and have analyzed the diffusion mechanism [20] by a combination of Density Functional Theory (DFT) calculations and kinetic Monte Carlo (kMC) simulations. Methekar et al. [21] performed kMC studies of the solid-electrolyte-interphase (SEI) formation on graphite electrodes. The effect of graphite and graphene edge morphology on diffusion was addressed by Leggesse et al. [22] with DFT calculations including Van der Waals interactions. The importance of kinetics within the Daumas-Hérold model (DH) in the staging phenomenon was highlighted by Krishnan et al. [23], also using DFT and kMC simulations. Smith et al. [24] have studied the dynamics of intercalation in layered materials with phase-fields models, focusing on the Li-ion/graphite system and very recently Chandesris et al. [25] have used a similar approach to simulate for the first time the complex staging kinetics between stage 3 and stage 2.

The exchange current $\dot{i}_0$ —or alternatively, the exchange current density $\dot{j}_0$—, is a useful kinetic parameter that enables analysis of the interfacial phenomena at steady state (zero current). Chang et al. [26], for example, have studied the influence of solvent composition, electrolyte concentration, storage time, and intercalated state on $\dot{i}_0$ and on other kinetic parameters, while Methekar et al. [21] have considered the effect of $\dot{i}_0$ on the formation of the passive SEI layer. On the other hand, other authors have examined the effect of morphology and structural properties of the electrodes [27,28] on the kinetics of this system. However, we have only found few articles presenting $\dot{i}_0$ (or $\dot{j}_0$) as a function of lithium occupation for Li-ion/graphite systems [14,26]

While Grand Canonical Monte Carlo techniques have enabled calculation of the thermodynamic properties of the present system, like partial molar enthalpy and entropy [29,30], kMC has the advantage of considering also kinetic phenomena. In a previous work we have demonstrated the great potential of kMC simulations to study Li-ion/graphite systems [31]. In that work it was found that this technique allows to extend simulation time to the scale of seconds to study the Daumas-Hérold staging model [32], neglecting in the model the vibrational motion of particles [33,34]. This is very convenient, since it is well known that Li-ion intercalation in graphite is a very slow process: typical cyclic voltammetry sweep rates are 4 μV/sec, or less [5], which represents nearly 42 hours of experimental time in a typical potential window of 0.3 V.

The main aim of this work is to show that kinetic Monte Carlo simulations can be used as a tool for emulating the framework for different electrochemical techniques commonly used in the laboratory and can put an atomistic interpretation on experimental results obtained for lithium-ion insertion into graphite. To cover a thorough study of the Li-ion / graphite system, the Results section is divided into different sub-sections: cyclic voltammetry, potentiostatic steps, diffusion coefficients, and exchange current densities. The study of cyclic voltammetry yields an overall picture of (de)intercalation processes, and allows a first comparison between simulated data and experimental results.

Potentiostatic steps show how important it is to get insight into the kinetics and the electrochemical responses of such processes. The relevance of diffusion phenomena at different occupations of the systems is then analyzed. Finally, exchange current densities are evaluated and compared with predictions of simpler modeling and experimental results. Grand Canonical Monte Carlo simulations (GCMC) are used as a complementary tool to show some of the limitations of the static (equilibrium) approach. For the reader's comfort, a nomenclature table is provided in section S.1 of Supplementary Information.

2. Calculations: Theoretical model and kinetic Monte Carlo methods

A 3D lattice-gas model is used, consisting of 2D lattices containing triangular adsorption sites, piled up to simulate the graphite structure. A detailed description of this construction is given in Supplementary Information, section S.2.1.

To get equilibrium properties, like equilibrium voltammograms, Grand Canonical Monte Carlo (GCMC) simulations were used. Dynamic properties were obtained using kinetic Monte Carlo (kMC). The events allowed in the different types of simulations are described in Section S.2.2.

The interaction energies, which rule the evolution of the system, were considered through a Hamiltonian consisting of different energy terms, as proposed in reference [35]: one for Li-Li interactions in the same layer, first term on the rhs of equation (1), another term accounting for Li-Li interactions in different layers, second term on the rhs of equation (1) planes, and a third occupational term [29]:

$$H = \sum_{i}^{M}\sum_{j\neq i}^{N_{ip}}\frac{c_i c_j \varepsilon}{2}\left[\left(\frac{r_m}{r_{ij}}\right)^{12} - 2\left(\frac{r_m}{r_{ij}}\right)^{6}\right] + \sum_{i}^{M}\sum_{j}^{N_{op}}\frac{c_i c_j \kappa}{2}\left(\frac{r_b}{r_{ij}}\right)^{\alpha} + (\gamma - \mu)\sum_{i}^{M}c_i \tag{1}$$

In this equation M is the total number of insertion sites, N_{ip} is the number of neighbors in the same layer, N_{op} is the number of neighbors in different layers, c is an occupational

variable for each site (0 empty, 1 full), ε is the potential depth at distance r_m, r_{ij} is the distance between Li ions occupying sites i and j, κ controls the repulsive interaction while α fixes the range of this repulsion, r_b is a distance, μ is the chemical potential (proportional to electrode potential E vs. Li / Li$^+$, as $\mu = -eE$) and γ is an energy scaling parameter. The cutoff distance at the XY plane is 10.0 Å, while the cutoff at the Z axis is 6.0 Å. This Hamiltonian and its modifications have allowed to perform different studies for the Li-ion/graphite [30,31,36]. In summary, equation (1) involves attractive interactions for lithium ions placed in the same layer with second and farther than second neighbors, and highly repulsive interactions with first neighbors. On the other hand, the interaction energy between Li ions placed in different layers is always repulsive. It must be acknowledged that equation (1) remains a heuristic approximation. In fact, Juarez et al. [37] have recently shown that the Li-Li interaction mediated by a carbonaceous substrate exhibits a considerably complexity that deserves further first-principles studies to be completely understood.

The dynamic hierarchy required for the events occurring in kMC simulations was established in a way similar to that in our previous work [31], as originally implemented in ref [38,39]. The latter two references discuss how to construct a Monte Carlo dynamics which simulates that of the real system under consideration, starting from a thermodynamic description of the system. It consists in using Arrhenius and Butler-Volmer approximation terms. These equations are detailed in Supplementary Information, section S.2.3. Thus, the rates Γ for the different events of the present simulations are given by:

$$\Gamma = v_0 \exp\left(-\frac{\Delta^*_\sigma}{k_B T}\right) \exp\left[-\frac{\alpha_{BV}(H_F - H_I)}{k_B T}\right]$$

(2)

where v_0 is a pre-exponential factor, H_I and H_F are the energies calculated with the Hamiltonian from equation (1) for the initial and final state respectively, k_B is Boltzmann constant, and T is the absolute temperature. Unless otherwise stated, $T = 296\,K$. Δ^*_σ is

7

the energy barrier for event σ ($\sigma = diff$ for diffusion and $\sigma = i/d$ for a particle insertion or deinsertion) and $\alpha_{BV} = 1/2$ the symmetry factor for charge transfer.

To perform GCMC, the usual Metropolis algorithm was applied [40] and 1×10^7 MC steps were needed to ensure energy convergence. Regarding kMC, the rejection-free kMC algorithm was used [33]. Any other computational considerations that concern the adaptation of the model to electrochemical techniques will be detailed in the corresponding section. We use the usual electrochemical convention, where oxidation currents are positive while reduction ones are negative.

3. Results and discussion

As stated in a previous work [31], the energy barrier $\Delta^*_{i/d} = 0.655\,eV$ was fitted to get the experimental exchange current density [26] at half occupation of the lattice. This yielded results comparable with other experimental work [41–43]. The diffusion barrier $\Delta^*_{diff} = 0.370\,eV$ was fitted using random walk theory and kMC simulations in the canonical ensemble for a single particle, such as to emulate the experimental results in the limit of low occupations [15]. $v_0 = 1\times10^{13}\,s^{-1}$ was assumed as proposed in ref [19,44]. The Hamiltonian parameters used were taken from [29] and are detailed in Table 1. Unless otherwise stated, $T = 296\,K$.

Table 1: Parameters introduced in the Hamiltonian of equation (1)

| $\varepsilon\ [eV]$	$r_m\ [\mathring{A}]$	$\kappa\ [eV]$	$r_b\ [\mathring{A}]$	α	$\gamma\ [eV]$
0.0255	4.26	0.255	1.42	4	−0.03

3.1. Cyclic voltammetry

A few modifications were introduced into the kMC code to simulate cyclic voltammetric profiles [45]. The parameters required are the potential sweep rate, v_{sr}, the initial potential value, E_0, and the final potential E_f. The changes required in the computer code and other details are described in section S.3.1 of Supplementary Information.

Since the simulated system is much smaller than the real one, it comes out that the sweep rates that may be used are considerably larger than experimental ones. For example, while Levi et al. [5], used sweep rates in the order of $\mu V\, s^{-1}$ for a system with a volume of 1.76×10^{-3} cm^3, our simulation system volumes are in the order of around 1×10^{-20} cm^3. Thus, the potential sweep rates that can be used to reach a steady state may, in principle, be much faster. We have considered ten potential sweep rates, going from the faster rates, where voltammetric peaks are not evident, to slower sweep rates, where the peaks are clearly defined. The potential window was between $E_0 = 120\ mV$ and $E_f = 65\ mV$. The reduction process (Li insertion) takes place in the linear potential sweep $E_0 \rightarrow E_f$ and the oxidation process (Li deinsertion) occurs in the positive potential sweep $E_f \rightarrow E_0$. The current is calculated as $i = Q\,\dfrac{dx}{dt}$, Q being the charge for the full graphite occupation and x the occupation of Li in graphite.

Figure 1a shows the simulated voltammograms and Fig 1b the occupations for different potential sweep rates. Comparison between these results and experimental measurements (Figure 1 from Levi and Aurbach [5]) denotes a qualitatively similar behavior, but it is due to different phenomena limiting lithium insertion in graphite, as discussed in Section S.3.2.

As the potential sweep rate is decreased, two peaks become evident in the negative and positive potential scans in Figure 1a. These peaks are labeled with i_{pr1} and i_{pr2} in the negative scan, and with i_{po1} and i_{po2} in the positive scan. Their potentials are denoted by $E_{pr1}, E_{pr2}, E_{po1},$ and E_{po2} respectively. Analysis of the system configurations, as discussed

below, indicates that the peak at E_{pr1} is related to the transition between the diluted stage I and stage II ($I_d \rightarrow II$), while the peak at E_{pr2} is evidence for the transition between stage II and stage I ($II \rightarrow I$). In general, a displacement of the oxidation peaks towards more positive potentials is observed as the sweep rate v_{sr} is increased and the oxidation current peaks become larger. On the other hand, the reduction peaks move towards more negative potential values under similar conditions.
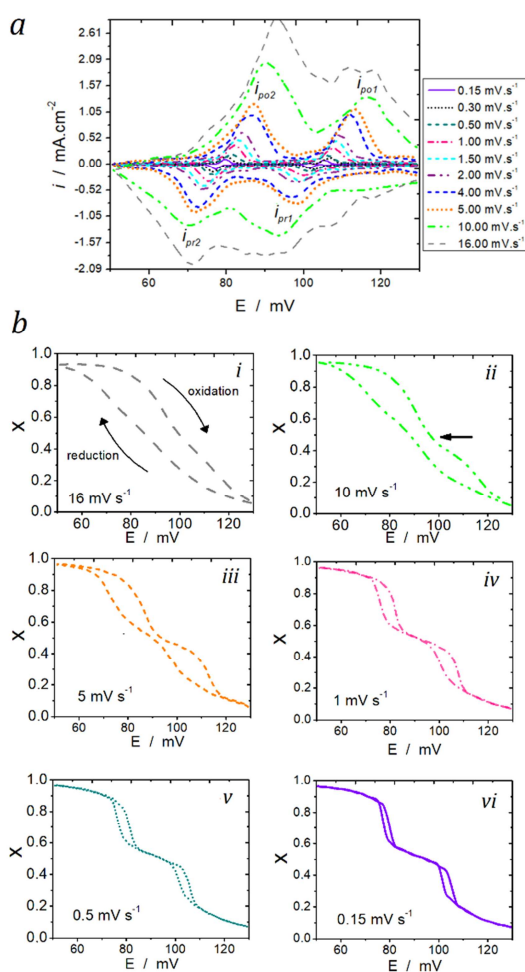
Figure 1: *a*) Cyclic voltammograms obtained with kMC simulations at different potential sweep rates, as indicated in the figure. *b*) Lattice occupation x, as a function of electrode potential, obtained from the integration of some of the voltammograms of Figure *a*. These figures aim to

illustrate the hysteresis between negative and positive potential scans. The potential sweep rates are indicated in figures *i - vi*.

Starting from low sweep rates, the reduction peaks i_{pr1} and i_{pr2} remain resolved until $v_{sr} = 5.0 \, mV.s^{-1}$, merging into a single peak at higher rates. The formation of stage II is not apparent under these conditions. The oxidation peaks i_{po1} and i_{po2} become indistinguishable at $v_{sr} = 16.0 \, mV.s^{-1}$. The question that arises is: Why do the reduction peaks merge sooner as the sweep rate is increased, as compared with the oxidation peaks? A possible answer is that the mechanisms of lithium intercalation and deintercalation may not be the same. Chronoamperometric experiments will help us later to delve deeper into the answer to this question.

Figure 1*b* shows the integral of the voltammograms for six different sweep rates, where the main changes can be appreciated. At the faster sweep rate, $v_{sr} = 16.0 \, mV.s^{-1}$, the two sigmoidal curves for insertion and deinsertion are separated by an important hysteresis loop. The arrows indicate the direction of the potential sweep rate for each process. This corresponds to the voltammogram in Figure 1*a*, where there is no evidence for peak separation at $v_{sr} = 16.0 \, mV.s^{-1}$. At $v_{sr} = 10.0 \, mV.s^{-1}$ a plateau in x starts to appear in the oxidative cycle (indicated by a black arrow), but it is not evident in the reductive one. In the rest of the curves with $v_{sr} < 10.0 \, mV.s^{-1}$ two plateaus are evident, and hysteresis between the curves becomes smaller, decreasing for lower sweep rates.

This hysteresis also becomes evident in the differences $\left| E_{po1} - E_{pr1} \right|$ and $\left| E_{po2} - E_{pr2} \right|$ as v_{sr} increases. As stated above, this was evident in the isotherms as a separation of the curves. This hysteresis, absent in GCMC simulations, is evidence for kinetic control. Slow kinetics due to particle exchange with the solution at the interphase, considered in our previous work, is a candidate for this [31].

11

A detailed analysis of the relationship between the peak current i_p and the sweep rate is carried out in Section S.3.2 of Supplementary Information, where the relationship between $\left| E_{po2} - E_{pr2} \right|$ and the sweep rate is analyzed in detail too.

As stated above, the sweep rates used in the present simulations are considerably larger than the experimental ones. In this respect, it is worth mentioning the voltammetric results recently obtained by Tao et al. in experiments for Li$^+$ ion insertion in LiMn$_2$O$_4$ single-particle systems [46]. These authors found that the sweep rates that can be applied to this system are several orders of magnitude larger than those used for ordinary (many-particles) electrodes. This suggests the possibility that nano-sized systems, like those simulated here, may allow Li$^+$ ion insertion at much higher rates than bulky ones do.

An analysis of voltammetric behavior for different system sizes is given in Supplementary Information, Section S.3.3.

3.2. Potentiostatic steps

Levi et al. [9] have analyzed experimental results obtained for the Li-ion/graphite system within the framework of Montella's contribution [10]. The latter author derived theoretical expressions for the response of ion-insertion electrodes to a potential step assuming Langmuirian conditions. Thus, before introducing the proper interactions formulated in the Hamiltonian (1), we have first validated our model with the simplified conditions from Montella. This validation is summarized in Section S.4 of Supplementary Information. We discuss here the results obtained with the full interactions model.

Potential steps were referred to the equilibrium voltammogram as calculated from GCMC simulations, shown in Fig 2. The potentials used to make potential steps are marked, being

$E_1 = 150\,mV$, $E_2 = 130\,mV$, $E_3 = 95\,mV$, $E_4 = 80\,mV$, $E_5 = 50\,mV$ all vs. Li/Li^+.
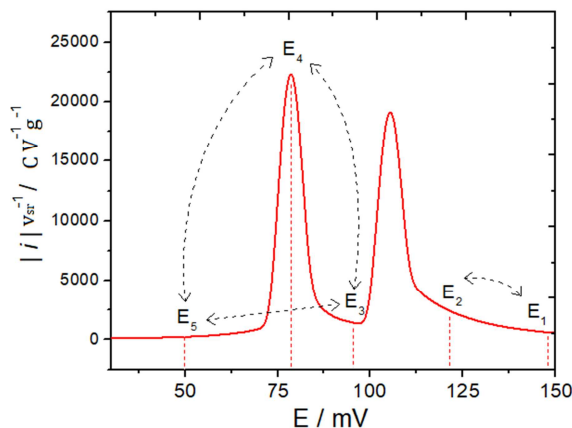
Figure 2: Equilibrium voltammogram obtained through GCMC simulations. This figure illustrates the potential values that were used to perform potentiostatic steps and obtain chronoamperometric transients. The values are denoted as E_1, E_2, E_3, E_4 and E_5, and are depicted in the figure. The arrows indicate the directions of the potential steps.

The arrows indicate the directions of the simulated potential steps from an initial potential to a final one, such that chronoamperometric experiments transients were obtained, similar to those of Levi et al. [9]. For the sake of getting reasonable statistics, it is not possible to make strict PITT simulations, which involve very small potential steps. However, it will be shown that many features of the simulated current-potential curves reflect the experimental results.

Before each potential step, the system was kept at the initial potential value until it reached steady state. Once this condition was achieved, the potential was stepped to the final value. The system size was 59.03 Å x 230.04 Å x 13.40 Å in the (X-Y-Z) directions.

The simplest case, where the same type of stage occurs before and after the potential step, will be analyzed first. Then, potential steps involving stage changes in intercalation and deintercalation simulations will be analyzed.

Simplest case: Potential step $E_1 \rightarrow E_2$

13

This potential step is undertaken between two potentials where there is no stage coexistence, under conditions where only stage Id is present. The current response and different representations of the simulated current results are shown in Figure 3.
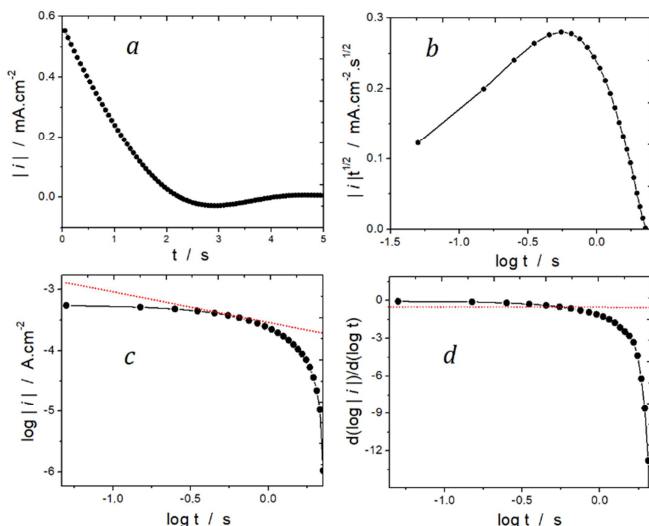
Figure 3: Simulation results for a $E_1 \rightarrow E_2$ potential step. In figure *c*) the red line is the tangent to the curve corresponding to the time of the maximum in Figure *b*). In figure *d*) the red line is the value of the slope of the tangent drawn in figure *c*). The magnitude represented in each plot is shown in the corresponding ordinate.

As found by experimental results for similar conditions from the literature (see Figure 2 from [9]), there is a single peak in the $|i|t^{1/2}$ vs. $\log t$ representation, Figure 3*b*, which was explained by the relatively slow charge transfer at the graphite/solution interphase. This is, in fact, the case in the present simulations, since the activation energy for charge transfer ($\Delta^*_{i/d} = 0.655 \, eV$) is relatively large as compared with the diffusion barrier ($\Delta^*_{diff} = 0.370 \, eV$ in the limit $x \rightarrow 0$). Furthermore, in Figure 3*c* there is a point that corresponds to the maximum value of $|i|t^{1/2}$ in Fig 3*b*. At that point, the slope of the tangent line, presented with a red dashed line, is -0.5 (the latter is shown in Figure 3*d*). Similar results were observed and described by Levi et al. [9] and confirm the equivalence

14

of both representations in the present case, i.e. when only one stage occurs in the region selected to take the potential step.

Intercalation case: Potential steps $E_3 \rightarrow E_5$ and $E_3 \rightarrow E_4$

This case involves two types of insertion potential steps (see Figure 2) starting from the same conditions. In the first one the system goes from stage II, at E_3, to a potential E_5 where stage I is completely formed under steady state conditions. In the second one, the final potential E_4 corresponds to one where stage I is only partially formed under steady state conditions.

Let us discuss first the bigger step $E_3 \rightarrow E_5$, where a faster insertion rate is expected, since the final potential E_5 is more negative than E_4. Figure 4a shows the lithium fraction, x, as a function of time, Figure 4b depicts the current i response, and Fig 4c shows $|i|t^{1/2} \, vs \, \log t$.
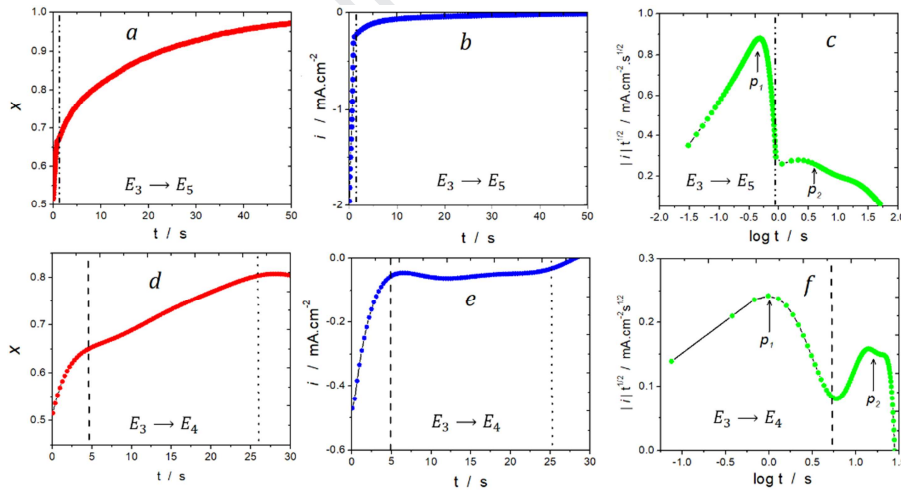

Figure 4: kMC results for the potential step $E_3 \rightarrow E_5$ (*a, b* and *c*) and $E_3 \rightarrow E_4$ (*d, e, f*). From left to right, the plots present lattice occupation x, current i and $|i|t^{1/2}$ as a function of time

The representation $|i|t^{1/2}\ vs \log t$ in Figure 4*c* shows two peaks, p_1 and p_2, separated by a minimum. The position of the latter is marked with a dot-dashed line that corresponds to the dot-dashed lines in Figure 4*a* and 4*b*. At the beginning, there is a large rate of ion insertion into graphite, which is evident in a fast change of x with time in Figure 4*a* and a fast change in i with time in Figure 4*b*. At approximately $t \approx 1\,s$ (dot-dashed line) there is an abrupt change in the responses of composition and current. From that moment on, ions are inserted more slowly and at $t = 50\,s$ the current has practically dropped to 0. The previous analysis shows that the changes of the behavior in x and i are related to the $|i|t^{1/2}$ minimum. p_1 is remarkably larger than p_2. An explanation for this difference will be given later.

We can go deeply into the mechanism that governs the evolution of the system by inspecting the simulation frames in Figure 5.
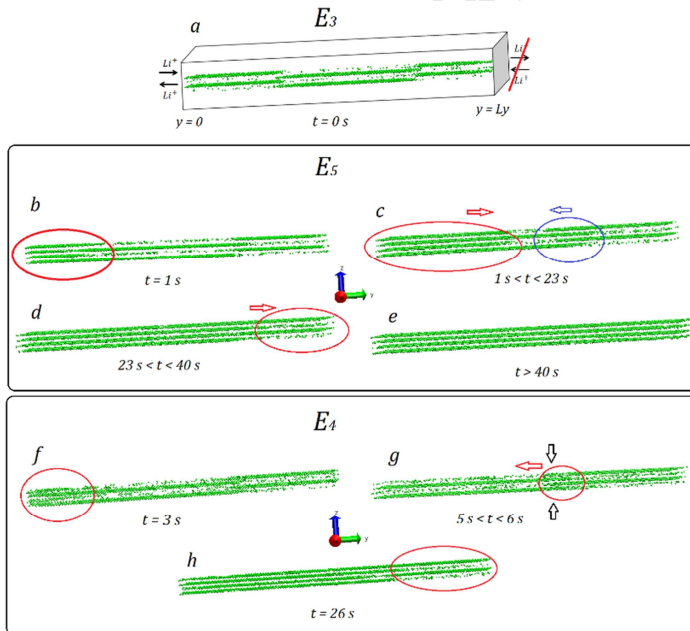
Figure 5: Frames from kMC simulations corresponding to Li-insertion steps, at the different times shown in the figure. Lithium-ions are represented in green and the graphite substrate is not shown. The box details are shown in Figure *a*. Red arrows indicate the direction and evolution of

the moving boundaries. The initial potential (E₃) is indicated at the top of the figure, while the final potentials for the rest of the frames (*b, c, d, e, f, g* and *h*) are indicated inside each box.

There, the graphite/electrolyte interphase is on the left of the simulation box ($y = 0$), denoted by two black arrows that represent Li exchange, and the closed end of the electrode is on the right ($y = L_y$, marked with strike-through arrows). Initially, at $t = 0\,s$ (Figure 5*a*), and just before each potential step, the system starts with the typical defective stage II structure, presenting DH (defective) domains.

Considering step $E_3 \rightarrow E_5$, when time starts to run, there is a fast ion insertion with the formation of a portion of stage I at the interphase (red circle at Figure 5*b*, $t \approx 1\,s$), which corresponds to the $|i|t^{1/2}$ minimum in Figure 4*c* and the concomitant changes in the behavior of x and i in Figures 4*a* and 4*b* respectively. This portion of stage I grows towards the inner part of the electrode as time passes (Figure 5*c*), while another portion of stage I is formed inside graphite, advancing in the opposite direction (blue circle). When the system reaches $t = 23\,s$ (Figure 5*d*), the current is practically zero, so the system is very close to steady state. In fact, in this situation there is a portion of stage II that seems to be difficult to remove (red circle), so it takes the system almost 15 more seconds to do it (Figure 5*e*). A dynamic picture of this process can be found in Supplementary Information, where a video illustrating this potential jump is available (KMC-Li-E3-E5.mp4). Each frame corresponds to an increment of $t \approx 1\,s$. These features can be understood as follows: as the stage I portion remains and grows from the interphase towards the inner part of the electrode, new ion insertion becomes difficult, making this process slower. Thus, the piece of stage I acts as a clog on Li-ion insertion. At this point it is pertinent to mention the conclusions drawn by Inaba et al. [47], who studied lithium intercalation into graphite by using in situ Raman spectroscopy. These authors found a change in the open circuit potential (OCP) towards higher values when they interrupted the charging negative current, together with spectroscopic evidence that the intercalate was evolving towards a

higher staging. Thus, they concluded that the electrode potential is determined by the surface stage. Figure 5*b* provides clear evidence supporting this hypothesis: while the interphase region presents stage I (red circle), the inner part of the electrode presents a Daumas-Herold stage II. Bringing the system to OPC (no current flow) would lead to a highly defective stage II. Snapshots of such a simulation are given in Supplementary information: KMC-Li-current-zero.mp4.

For the smallest step $E_3 \rightarrow E_4$, if the x and i responses are compared with those obtained in the $E_3 \rightarrow E_5$ potential step, it can be seen that the initial ion insertion speed is slower in the first case, as expected. Surprisingly, however, it takes about 20 seconds less than the largest step to reach steady state ($i = 0 \, Ag^{-1}$). The $\left| i \right| t^{1/2} \, vs \, \log t$ plot of Figure 4*f* shows another remarkable difference with respect to that in Figure 4*c*. The height difference between p_1 and p_2 becomes smaller for $E_3 \rightarrow E_4$, p_1 being remarkably lower as compared with the larger potential step.

The initial configuration for step $E_3 \rightarrow E_4$ is the same as that for $E_3 \rightarrow E_5$ (Figure 5*a*). Then, at $t \approx 3s$ a clog denoted by a red circle in Figure 5*f* appears, corresponding to the time point where the sudden change in x and i occurs (dashed line in Figure 4*d* and 4*e*). This corresponds to the minimum in $\left| i \right| t^{1/2}$ (dashed line in Figure 4*f*). As it can be seen, the ions nucleate next to the interphase to arrange in a small stage I domain (red circle), clogging the interphase for further ion insertion. Then, the clogging domain disappears relatively fast, in less than a second, to form a structure like that in Figure 5*g*. Particle insertion proceeds moving the boundaries in the direction of the interphase, as indicated by the horizontal arrow, with the formation of a fragment of stage I (vertical arrow and red circle) that grows between two stage II portions (one near the interphase and another one at the closed end of the electrode). At $t \approx 27s$ the system reaches the structure shown in Fig 5h, where the system cannot easily eliminate the portion of stage II located far away from the interphase (red circle). A video of the process is available in

Supplementary Information, KMC-Li-E3-E4.mp4. Each frame there corresponds to time increments of $0.66\,s$.

Deintercalation case: Potential steps $E_5 \rightarrow E_3$ and $E_4 \rightarrow E_3$

Two types of deintercalation simulations will be analyzed. As in the insertion case, the biggest step $E_4 \rightarrow E_3$ will be analyzed first (Figures 6*a*, 6*b* and 6*c*).
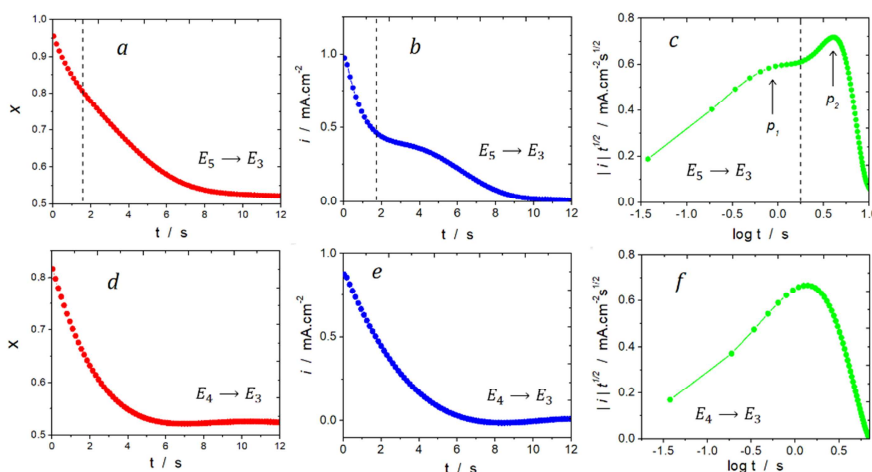
Figure 6: kMC results for the $E_5 \rightarrow E_3$ (*a, b,* and *c*) and the $E_4 \rightarrow E_3$ (*d, e, f*) deintercalation steps.

At the beginning, $t \approx 1.8\,s$, marked with a dashed line in Figures 6*a* and 6*b*, ions deintercalate fast from graphite. This can be visualized in the behaviors of both i and x versus time. After $t = 1.8\,s$, the change in i becomes slower, showing a shoulder around $t \approx 4\,s$ and presenting then a monotonous decrease. Close to the end of the transient, at $t \approx 8\,s$, there is a final inflection in i before reaching the steady state. The $\left|i\right|t^{1/2}$ plot (Fig 6*c*) shows two merged peaks where, opposite to the insertion case, the first (p_1) is smaller than the second one (p_2). The inflection between both peaks, marked with a dashed line, coincides with the points in x and i, marked with dashed lines too. It is

remarkable how these transients are different from those of the insertion case $E_3 \rightarrow E_5$, especially for the third set of plots, where p_1 is now smaller than p_2.

The deinsertion mechanism developing in $E_5 \rightarrow E_3$ can be properly understood by the analysis of the corresponding snapshots: Figure 7a shows the initial stage I arrangement (corresponding to the steady state at potential E_5) with the box details included as in Figure 5a, to remind the reader of the restrictions imposed to the system. Immediately after the potential step, the system generates several holes, creating a portion of stage II next to the interphase, which is marked with a red circle in Figure 7a. Again, as in the intercalation case, the initial formation of stage II next to the interphase (stage I in intercalation) is in agreement with the proposal of Inaba et al. [47], namely that the electrode potential is determined by the surface stage. Once stage II has been formed, the defects propagate into the electrode (as red arrows indicate), as ions are being removed from the system (Figure 7c). Finally, a portion of stage II (red circle) get stuck at the end of the electrode and seems to be removed very slowly (its removal taking longer than the whole simulation time). Thus, the formation of stage II in this simulation involves three well differentiated steps: a) creation of the first defects; b) propagation of these defects; c) reaching of the steady state. This coincides with the three different behaviors observed in the current transient: a) initial current drop ($0s < t < 1.8s$); b) current arrest, ($1.8s < t < 8.0s$); and c) final drop of the current ($t > 8.0s$). The transition between the a) and b) regimes corresponds to the dashed line separating the shoulder and the maximum in $\left| i \right| t^{1/2}$ plot (Figure 8c). Supplementary Information shows a video corresponding to this potential step: KMC-Li-E5-E3.mp4. Each frame corresponds to a time increment of $0.24s$.

Comparing these results with the insertion simulations, it is clear that the deinsertion rate for $E_5 \rightarrow E_3$ ($I \rightarrow II$) is faster than the insertion rate for $E_3 \rightarrow E_5$ ($II \rightarrow I$) (it takes 8 s vs. 35 s respectively, to reach the steady state). This is not a trivial result, and it must be emphasized that Levi et al. [11] drew the same conclusion through their experiments. This broadly suggests that nucleation plays different roles in deinsertion and insertion.

For the potential step $E_4 \rightarrow E_3$, (Figures 6*d*, *6e*, and *6f*), there is only one peak in the Cottrell representation. Then current and lithium fraction have monotonic behaviors as a function of time. This situation is the same as that found in the potential step without stage coexistence (Figure 3). Comparison between the $E_4 \rightarrow E_3$ transient and the $E_5 \rightarrow E_3$ one, shows that there is not peak multiplicity in $\left| i \right| t^{1/2}$ *vs* $\log t$ (Figure 6*f*) in the second case.
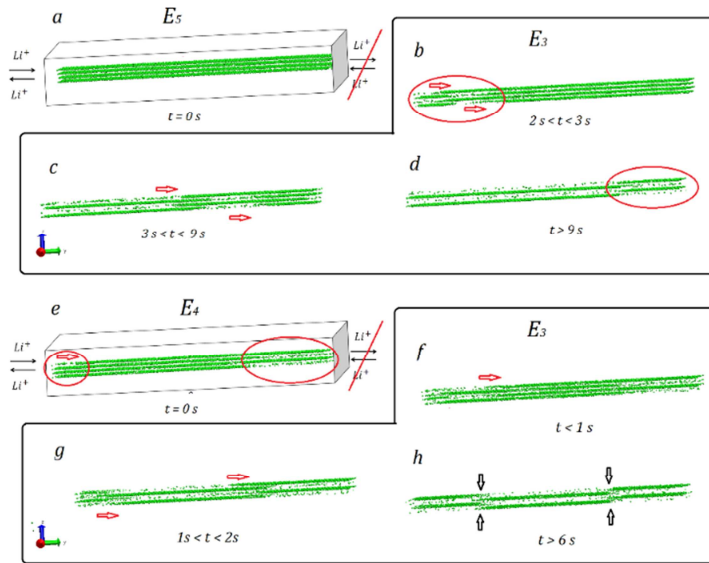
Figure 7: Simulation frames for deintercalation. The box details are shown in Figures *a* and *e*, but the conditions imposed apply for all frames. To improve visualization of the phenomena, the graphite substrate is not shown. Red arrows indicate the direction of the moving boundaries. The initial potential is indicated at the top of Figures *a* and *e*, then the final potential for the rest of the frames (*b, c, d, f, g*, and *h*) is indicated inside the limits of the big box.

Looking at the frames for this potential step (Figures 7*e*, 7*f*, 7*g* and 7*h*) the first thing that can be noted is that the initial configuration (Figure 7*e*) is not a pure stage I. The red circles indicate half-filled portions of the system: next to the interphase there is a partially empty layer and at the other end of the electrode, a considerable portion of stage II is present. The other remarkable fact is that, although both potential steps reach the same

final potential E_5, approximately half of the times the configuration from the initial potential E_4 presents several mismatches (Figure 7h). This is not the case, of course, for the configurations starting from the potential E_5, where all configurations correspond to the perfectly ordered Stage I (Figure 7a). This difference is easy to understand if we think that, when starting with a pure stage I configuration, the system can only eliminate particles in one direction (in the direction of the interphase, where holes are constantly being generated). On the other hand, when starting with a mixed-stage coexistence configuration, the system moves particles in different directions, reaching different metastable states with a different number of mismatches when different simulations are run. Supplementary Information shows a video file of this potential step: KMC-Li-E4-E3.mp4. Each frame corresponds to an increment of $t \approx 0.13s$.

A discussion connecting the results of Cyclic Voltammetry and Chronoamperometry is provided in Section S.4. There we explain the reasons for the differences found between intercalation and deintercalation, in the $\left| i \right| t^{1/2}$ vs $\log t$ representation. In short, p_1 is related to Li (de)insertion, while p_2 is controlled by diffusion.

3.3. Li-ion Diffusion in Graphite

Chemical diffusion coefficients (D) are usually obtained with simulation methods that deliver mean-square displacements and the thermodynamic factor (Θ) for different lithium occupations, see equation (3). Then, the diffusion coefficient is obtained using the so-called Kubo-Green formula [48]:

$$D_{Li} = \Theta D_j = \frac{1}{2d} \left(\frac{\langle (\delta N)^2 \rangle}{\langle N \rangle} \right)^{-1} \left\langle \left(\frac{1}{N} \sum_{i=1}^{N} \Delta r_i \right)^2 \right\rangle \tag{3}$$

where $\langle (\delta N)^2 \rangle \cdot \langle N \rangle^{-1} = \Theta^{-1}$ is the normalized mean-square fluctuation, Δr_i is the displacement of the ith particle at time t, and d is the system dimension. From a

22

thermodynamic viewpoint, the thermodynamic factor is related to the insertion isotherm and the chemical potential μ according to:

$$\Theta = \left(\frac{\partial \left(\mu / k_B T \right)}{\partial \ln x} \right)_T \qquad (4)$$

where k_B is the Boltzmann constant and T is the absolute temperature. For this reason, it is well known that the calculation of Θ is difficult for phase transitions where there is phase coexistence [48,49]. This is so because if the change of x with μ becomes steep, as is the case of a first-order phase transition, Θ in principle should diverge. GCMC equilibrium isotherms for lithium insertion in graphite show abrupt lithium composition jumps from a stage to another due to particle condensations, so that Θ calculation becomes problematic from a GCMC approach, and so does the calculation of diffusion coefficients at different x. In fact, there are not many theoretical works dealing with this subject. Furthermore, we have recently shown that Li$^+$ insertion kinetics generates metastable defective (Daumas-Herold structures), so that measured values do not strictly correspond to those of equilibrium states. To solve this problem and to come closer to the experimental situation, we propose here to calculate the diffusion coefficient from equation (3) [48], but using theoretical equations of jump diffusion coefficients (D_j) and obtaining Θ by taking the derivative of the simulated isotherms for a slow potential sweep rate, where metastable (Daumas-Herold) structures occur. Thus, within the present approach D_{Li} is calculated from:
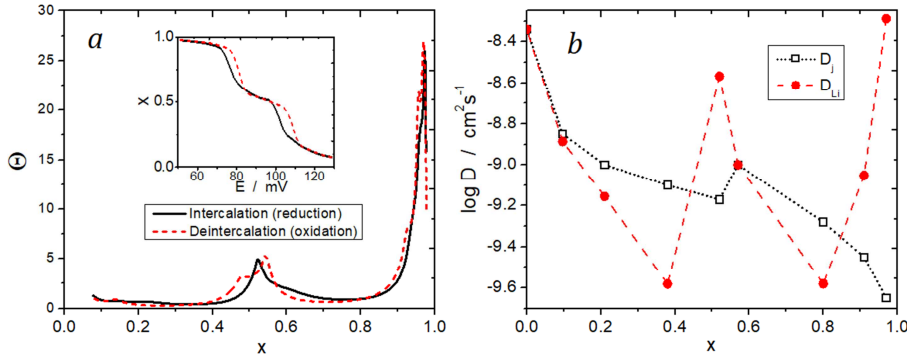
$$D_{Li} = \left(\frac{\partial (\mu / k_B T)}{\partial \ln x} \right)_T D_j \qquad (5)$$

Where

$$D_j = \frac{1}{2d} \langle \Gamma \rangle \lambda^2 \qquad (6)$$

and $\langle \Gamma \rangle$ is the average value of the jump rates over all particles and λ is the characteristic jump distance.

23

Figure 8: a) Thermodynamic factor Θ obtained from cyclic voltammetry data according to equation (4). The inset shows the isotherm for the slow sweep rate used. b) Jump diffusion coefficients D_j (in black), calculated with equation (6) and chemical diffusion coefficients D_{Li} (in red), calculated with equation (5), obtained with canonical kMC simulations.

D_j values were obtained from kMC simulations carried out in the canonical ensemble. The system size was the same as that used for the CV simulations. Each point of the plot $\log(D)$ *vs* x was obtained by the following procedure: first, a chronoamperometric simulation was run at a selected electrode potential, where a given x value was obtained at steady state (SS). After the system reached the SS, a typical configuration was used to launch the canonical ensemble to calculate the average $\langle \Gamma \rangle$.

The thermodynamic factor Θ was obtained by taking the derivative from the isotherm simulated at a slow sweep rate from cyclic voltammetry experiments. The corresponding x vs. μ plot is shown in the inset of Figure 8*a*, while Θ is shown in Figure 8*a*. In this case Θ was calculated from data for the intercalation process. Using deintercalation data delivers similar results, with a small hysteresis.

Figure 8*b* shows $\log(D)$ *vs* x, empty squares represent D_j, and red circles, D_{Li}. An absolute maximum is found in D_j for $x \rightarrow 0$. Then, it decreases for larger x, with a small step at $x \approx 0.5$. The behavior of D_j is a consequence of the changes in the average jump

rate with occupation (see equation 6). As lattice occupation increases, attractive interactions between particles slow down particle diffusion, so, as a general trend, D_j decreases with increasing occupation. However, at $x \approx 0.5$ an order-disorder transition occurs [50–52]. This transition is a consequence of the repulsive interactions between ions in different layers: at very low occupations all layers are filled more or less homogenously but, at some point, repulsive interactions between neighboring layers lead to Stage II (more properly stated, to a DH defective stage II). As stage I begins to be formed from stage II at $x \approx 0.5$, an effective repulsive interaction between particles arises, leading to a small increase in D_j, as observed. To schematize how interactions evolve, a plot of the partial molar energy $\frac{\partial E_{Li}}{\partial x}$ as a function of occupation is shown in the Supplementary Information Figure S8 in Section S.6. E_{Li} denotes the energy per Li ion particle. It is remarkable how $\frac{\partial E_{Li}}{\partial x}$ rises when stage II is formed, due to repulsive interactions.

A first inspection of the plots in Figure 8b shows a remarkable similarity with the results presented in Figure 6 in ref. [15]. The diffusion coefficients D_{Li} from the present simulations are comparable with those obtained from PITT experiments, where maxima are observed at occupation values corresponding to pure stages compositions and for $x \rightarrow 0.0$, while minima are found for intermediate lithium compositions. On the other hand, the results for D_j resemble the diffusion coefficients obtained from EIS classical formula, where minima are found at occupation values corresponding to pure stages, that is, $x = 0.5$ and $x \rightarrow 1.0$. However, in this case, a correlation cannot be claimed since experimental results should reflect the values of the chemical diffusion coefficient and not those of D_j.

3.4 Exchange Current Density

To obtain exchange current densities, j_0, for different compositions of Li in graphite, x, two different approaches were used, which will be denoted with *static and dynamic*. j_0 was obtained by dividing the exchange current i_0 by the cross-sectional area $A_{xz} = L_x \times L_z$ (mA.cm^{-2}).

In the case of the *static* approach, chronoamperometric simulations were performed at different electrode potentials, letting the system evolve towards the steady state. Under the latter condition, the number of inserted and deinserted ions per unit time becomes equal and therefore the net Li-ion flow across the interphase becomes zero. This fact can be stated in terms of the oxidation current i_{ox} and the reduction current i_{red}. Thus, at the steady state $i_0 = |i_{red}| = i_{ox}$, i_{red} and i_{ox} being the reduction and oxidation currents respectively. We use the usual electrochemical convention, where oxidation currents are negative while reduction currents are negative. A graphic illustration and a more detailed explanation is given in Section S.7.1, Supplementary Information.

Sequences of chronoamperometric simulations were performed in both directions, intercalation and deintercalation, and the j_0 values were obtained from an average of both simulations. Figure 9*a* presents a plot of j_0 *vs* x as obtained from these simulations. It is evident that j_0 rises from $x = 0$ until $x = 0.2$ (zone *I*). Then, there is no significant j_0 change in the range $0.2 \le x \le 0.8$(zone *II*), and for $x > 0.8$ (zone *III*) j_0 decreases with x until reaching a minimum value at maximum Li occupation.

The qualitative aspects of Figure 9*a* can be rationalized by addressing the calculation of the exchange current density in terms of a Butler-Volmer/Frumkin isotherm, as formulated by Levi and Aurbach in reference [5]. After the mathematical treatment of data included in section S.7.2 Supplementary Information, it is found that:

$$i_0 = Q k_1^{0.5} k_{-1}^{0.5} c_{Li^+}^{0.5} \left(1 - x\right)^{0.5} x^{0.5} \tag{7}$$

where Q denotes the charge corresponding to full occupation of the system ($x=1$), k_1 and k_{-1} are forward and reverse rate constants respectively, and c_{Li^+} is the Lithium-ion concentration in the solution.
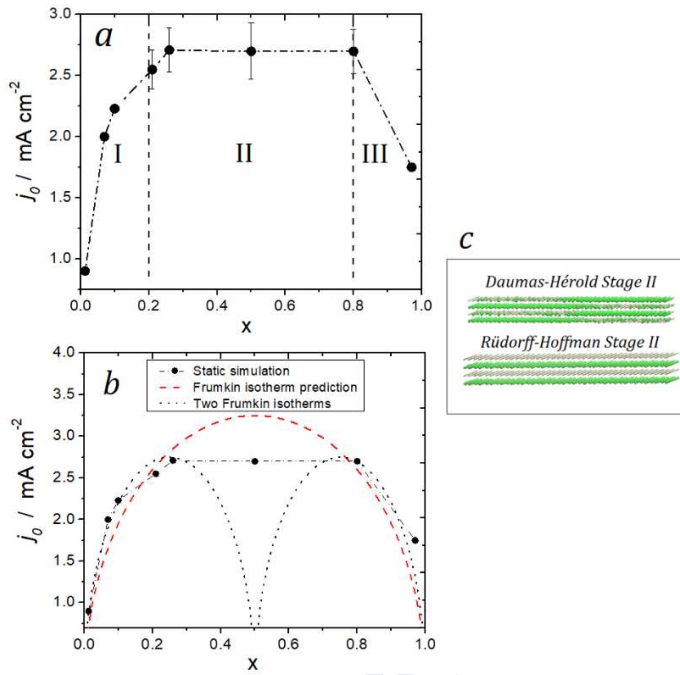
Figure 9: *a*) Exchange current density calculated by the *static* approach described in the text, using potentiostatic steps. *b*) comparison of figure b) results with the prediction of the Frumkin isotherm, Equation (7), and with the assumption of two separate Frumkin isotherms. *c*) Top: Snapshot of a simulation where j_0 was calculated for $x = 0.5$. Bottom: "Perfect" Rüdorff-Hoffmann structure for stage II. Note the difference between this ideal structure and that of the Daumas-Herold type, on top.

The prediction of equation (7) is plotted in Figure 9*b* in a red dashed line, together with the simulated results in black circles, where qualitative similarities may be drawn. The Frumkin isotherm prediction has been applied by Dees et al. [53] to discuss the exchange current of a nickel oxide positive electrode and by Ecker et al. [54], who presented results for graphite. Figure 9*b* also shows the j_0 prediction assuming two separated Frumkin isotherms (black dotted line), one for the formation of stage II and another one for the

formation of stage I. It can be appreciated that the latter curves follow the simulated data more closely, denoting the complex nature of the present phenomenon. This is expected, since in a rough approximation, and neglecting higher order staging, two main components are observed in voltammetric peaks, which correspond to the formation of stages II and I. However, the striking difference that we find between the simulated j_0 results and the two-Frumkin isotherm behavior is that, while the former is flat around $x = 0.5$, the latter shows a minimum at that point. The latter prediction is understandable: a perfect Rüdorff-Hoffmann (RH) stage II model [55] is the alternated combination of two structures: a Li-ion filled graphite slab, separated by nearly empty graphite slabs. The exchange current density expected for this type of structure is close to cero: the filled layers cannot accept further ions and the empty layers cannot deliver them. This is the prediction of (7) for both extremes, $x = 0$ and $x = 1$. The reason why the simulated j_0 does not drop to low values at $x = 0.5$ can be understood if we take a look at a snapshot of a simulation with $x = 0.5$ (see Figure 9c).

It can be observed that the simulated system (top) does not present a Rüdorff-Hoffmann (RH) stage II structure (bottom) but rather a typical Daumas- Herold (DH) structure, which are metastable states, as already discussed in ref [31]. Thus, ion exchange with the solution is not led by alternated filled/empty layers but rather by half-filled layers, as shown on the top of Figure 9c. As discussed in our previous work, DH structures [32] are the result of a slow equilibration with the solution, and the obtaining of the RH could be managed after extremely long simulation times, or by setting an artificially large exchange rate with the solution. To assess which would be the j_0 predicted by our simulations in the case of a perfect RH stage II structure, we have prepared such an RH structure and we have calculated its j_0 in two different ways. In the first of them, we have "frozen" the occupations of the alternate layers, performing the kMC simulation without allowing exchange with the solution. The j_0 obtained in this case was $0.23\,mA.cm^{-2}$. In the second, we allowed ion exchange with the solution. In this case, the resulting value was $j_0 = 0.40\,mA.cm^{-2}$. This is the value that would be obtained after an infinitely long

equilibration time at $E = 90\,mV$. So, if we put the latter result inside Figure 9*b*, the point at $x = 0.5$ will drop to a deep minimum like the prediction made using the two-Frumkin isotherms behavior. This shows the strong influence of kinetics on the present system, preventing it from reaching equilibrium.

In the case of the *dynamic* determination of the exchange current density, cyclic voltammograms were performed at 0.15 mV/s (the lowest sweep rate used in the present work), and the exchange current density was determined during the sweeps by counting the number of inserted/deinserted particles per unit time. Figure 10*a* presents the dynamic occupation of the lattice upon lithiation (black squares) and delithiation (red circles) scans, while Figure 10*b* shows j_0 determined during negative (black squares) and positive (red circles) sweeps.
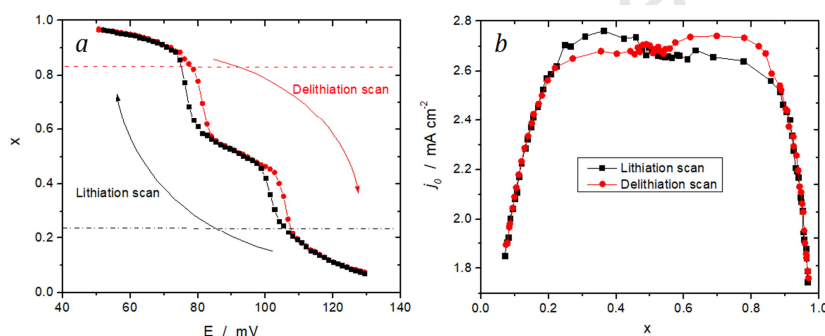
Figure 10: *a*) Lattice occupation during the intercalation (black) and deintercalation (red) sweeps used to determine the dynamic exchange current densities. v = 0.15 mV.s^{-1}. *b*) Dynamic determination of the exchange current density during negative (black) and positive (red) potential sweeps. Black and red points correspond to lithiation and delithiation sweeps respectively.

While the curve of the negative potential sweep (black squares) presents an overestimation of j_0 at low occupations, the opposite occurs in the positive potential sweep, where j_0 is overestimated for large x. To understand this effect, let us consider first a delithiation sweep (red squares). The reason for these overestimations may be understood looking at Figure S9*b*, in Section S.7.1. When graphite is being delithiated in a positive potential sweep, the positive current is larger than the negative current at each

stage, as it happens in Figure *S9b* at short times. This is so because for the lithiation current to increase, places need to be set free, something that only happens after delithiation. In other words, when the system is being delithiated, the lithiation current (negative) "follows" the delithiation current (positive). The opposite happens in a lithiation sweep: lithiation currents are "followed from behind" by delithiation currents, so non steady state measurements deliver larger exchange current density values.

Further understanding of the hysteresis in j_0 can be gained comparing Figure 10*a* and Figure 9*b*. The isotherm in Figure 10*a* shows hysteresis around 105 mV (stage II-stage Id transition) and around 80 mV (stage I-stage II transition). Let us consider a negative (lithiation) scan in the first region, ≈ 105 mV, at the composition marked with a black dot-dashed line ($x \approx 0.25$). At this point, the system has not entirely "left" stage Id during the negative scan, and it still shows a more or less homogeneous distribution of ions. The system follows this disordered (non-equilibrium) arrangement until $x \approx 0.40$. Thus, in the range $0.2 < x < 0.4$ the exchange current density rather follows the red curve of Figure 9*b*, the Frumkin prediction, which overestimastes j_0. As the Frumkin isotherm only considers an attractive parameter for Li interactions, it can be supposed that the ordering due to repulsive interactions, which leads to stage II defective structures, results in a decrease of j_0 at $x = 0.5$ in the simulation results. This situation differs from the maximum observed in the Frumkin model for the same Li occupation (Figure 9*b*) This hypothesis can be checked by performing a simulation without repulsive interactions, which is shown in Supplementary information, Section S.7.3, Figure S10, where it is observed that the behavior of the system in such conditions is more similar to that of the Frumkin isotherm. A similar argument can explain the hysteresis in j_0 in the positive sweep around 80 mV ($x \approx 0.83$), where the system has not entirely "left" stage I at the red dashed line.

From these latter results we can therefore conclude that experiments driven dynamically in a certain direction (negative or positive potential scans or sequences of potential steps) will deliver a j_0 overestimation. In this respect, it is interesting to revisit the j_0 results obtained in reference [14], replotted in Figure 11. These authors performed impedance

measurements to determine j_0, where the various x values were prepared by passing a given amount of cathodic charge. This situation is somehow comparable with a negative (lithiation) sweep. It can be noticed that both experimental and simulated results show a similar behavior in the intermediate occupation region.
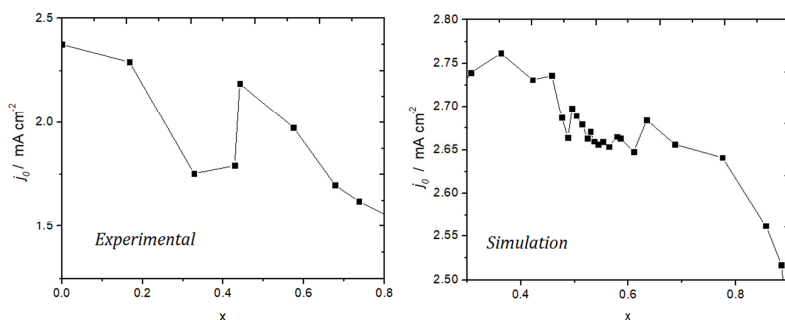
Figure 11: Comparison between the experimental exchange current density data from ref [14] and the dynamic simulation from Figure 10*b* for the lithiation process.

4. Conclusions

The present work applies the kinetic Monte Carlo technique to deal with different aspects of Li-ion insertion in graphite.

Cyclic voltammograms and lattice occupations at different potential sweep rates were simulated and compared with experimental data. The behavior of the current peaks and the difference between the reduction and the oxidation peak potentials were analyzed as a function of the potential sweep rate, for the $II \leftrightarrow I$ transition peaks., The simulation resembles the experimental results in several aspects.

Regarding the simulation of potentiostatic steps, the model was first validated by setting Langmuirian conditions, yielding the theoretical predictions of ref [10]. This step was important to show that the lattice model yields the same result as a well-established continuum modeling under these limiting conditions. After this validation, potentiostatic step experiments for intercalation and deintercalation of Li in graphite were simulated. The qualitative behavior of the current and $it^{1/2}$ were the same as those found in

experiments: only one peak appears in the $it^{1/2}\,vs\,\log t$ plot when the same stage is present before and after the potential jump, while two peaks are found when a different stage is formed after the potential step. The reason for the occurrence of the two-peaks was explained with the aid of simulation snapshots. The first peak was related to charge transfer control, while the second, occurring at longer times, was found to be ruled by mixed charge transfer and diffusion.

The reason why deintercalation is faster than intercalation was also explained: a clog is formed at the graphite/solution interphase during the intercalation potential steps.

Then, chemical diffusion coefficients for different Li occupations were obtained. To mimic the experimental procedure for their calculation, the thermodynamic factor was obtained from slow-sweep rate voltammograms. The behavior of the diffusion coefficient at different lattice occupations was explained in the framework of the interactions among the particles of the system.

Finally, exchange current densities for different Li occupations were obtained in two different simulation approaches, and compared with the predictions of one and two-Frumkin isotherms models. Comparison between the simulations and the latter case led to infer that the relatively high exchange current density observed in the simulations for stage II was due to the defective Daumas-Hérold arrangement. To check this point, simulations were run using a pure Rüdorff-Hoffman stage II structure. The result was a considerably lower exchange current value for half occupation of the lattice.

In summary, it can be stated that Kinetic Monte Carlo simulations appear as a useful tool to describe the electrochemical behavior of Li-ion insertion in graphite, with the advantage that they provide atomistic details on this phenomenon. The simulations performed provide understanding of experimental results obtained with different techniques, like cyclic voltammetry and potentiostatic steps, and they may also predict the behavior of the diffusion coefficient and the exchange current density as a function of different intercalation levels.

As future issues, two tasks emerge: the first is the improvement of the computer code to perform simulations for larger systems, approaching the microscale. This will provide a straightforward comparison with experiment. In this respect, it is worth mentioning that Tao et al. have performed voltammetric experiments with $LiMn_2O_4$ single-particle systems [46], with the finding that the sweep rates that can be applied are orders of magnitude larger than those used for ordinary (many-particles) electrodes. Similar experiments done with single-particle graphite electrodes could be compared directly with the results of the present simulations

The second problem to be addressed is the improvement of interaction potentials to describe other high-order staging phases. Recently, Mercer et al. [56] have found a way to theoretically reproduce the most positive couple of peaks for Li^+ insertion/deinsertion in/from graphite. This improvement should be introduced in the present kMC scheme.

Acknowledgements

References

[1]   J.O. Besenhard, The Electrochemical Preparation and Propereties of Ionic Alkali Meta-and NR4-Graphite Intercalation Compounds In Organic Electrolytes, Carbon N. Y. 14 (1976) 111–115. doi:https://doi.org/10.1016/0008-6223(76)90119-6.

[2]   M. Li, J. Lu, Z. Chen, K. Amine, 30 Years of Lithium-Ion Batteries, Adv. Mater.

1800561 (2018) 1–24. doi:10.1002/adma.201800561.

[3] J.R. Dahn, Phase diagram of LixC6, Phys. Rev. B. 44 (1991) 9179–9177. doi:https://doi.org/10.1103/PhysRevB.44.9170.

[4] T. Ohzuku, Y. Iwakoshi, K. Sawai, Formation of Lithium-Graphite Intercalation Compounds in Nonaqueous Electrolytes and Their Application as a Negative Electrode for a Lithium Ion (Shuttlecock) Cell, J. Electrochem. Soc. 140 (1993) 2490. doi:10.1149/1.2220849.

[5] M.D. Levi, D. Aurbach, The mechanism of lithium intercalation in graphite film electrodes in aprotic media. Part 1. High resolution slow scan rate cyclic voltammetric studies and modeling, J. Electroanal. Chem. 421 (1997) 79–88. doi:10.1016/S0022-0728(96)04832-2.

[6] M.D. Levi, C. Wang, D. Aurbach, Z. Chvoj, Effect of temperature on the kinetics and thermodynamics of electrochemical insertion of Li-ions into a graphite electrode, J. Electroanal. Chem. 562 (2004) 187–203. doi:10.1016/j.jelechem.2003.08.032.

[7] M.D. Levi, D. Aurbach, Simultaneous Measurements and Modeling of the Electrochemical Impedance and the Cyclic Voltammetric Characteristics of Graphite Electrodes Doped with Lithium, J. Phys. Chem. B. 101 (1997) 4630–4640. doi:10.1021/jp9701909.

[8] A. Funabiki, M. Inaba, T. Abe, Z. Ogumi, Stage Transformation of Lithium-Graphite Intercalation Compounds Caused by Electrochemical Lithium Intercalation, J. Electrochem. Soc. 146 (1999) 2443–2448. doi:10.1149/1.139195.

[9] M.D. Levi, E. Markevich, D. Aurbach, The Effect of Slow Interfacial Kinetics on the Chronoamperometric Response of Composite Lithiated Graphite Electrodes and on the Calculation of the Chemical Diffusion Coefficient of Li Ions in Graphite, J. Phys. Chem. B. 109 (2005) 7420–7427. doi:https://doi.org/10.1021/jp0441902.

[10] C. Montella, Discussion of the potential step method for the determination of the diffusion coefficients of guest species in host materials, J. Electroanal. Chem. 518

(2002) 61–83. doi:10.1016/S0022-0728(01)00691-X.

[11]   M.D. Levi, E. Markevich, D. Aurbach, Comparison between Cottrell diffusion and moving boundary models for determination of the chemical diffusion coefficients in ion-insertion electrodes, Electrochim. Acta. 51 (2005) 98–110. doi:10.1016/j.electacta.2005.04.007.

[12]   B.P. Freiländer, P. Heitjans, H. Ackermann, G. Kiese, H. Stöckmann, C. Van Der Marel, Diffusion Processes in LiC6 Studied by B-NMR *, Zeitschrift Für Phys. Chemie Neue Folge. 101 (1987) 93–101. doi:https://doi.org/10.1524/zpch.1987.151.Part_1_2.093.

[13]   P. Yu, B.N. Popov, J.A. Ritter, R.E. White, Determination of the Lithium Ion Diffusion Coefficient in Graphite, J. Electrochem. Soc. 146 (1999) 8–14. doi:10.1149/1.1391556.

[14]   T. Piao, S. Park, C. Doh, S. Moon, Intercalation of Lithium Ions into Graphite Electrodes Studied by AC Impedance Measurements, J. Electrochem. Soc. 146 (1999) 2794–2798. doi:10.1149/1.1392010.

[15]   M.D. Levi, D. Aurbach, Diffusion coefficients of lithium ions during intercalation into graphite derived from the simultaneous measurements and modeling of electrochemical impedance and potentiostatic intermittent titration characteristics of thin graphite electrodes, J. Phys. Chem. B. 101 (1997) 4641–4647. doi:10.1021/jp9701911.

[16]   M.D. Levi, G. Salitra, B. Markovsky, H. Teller, D. Aurbach, U. Heider, L. Heider, Solid-State Electrochemical Kinetics of Li-Ion Intercalation into Li1−xCoO2: Simultaneous Application of Electroanalytical Techniques SSCV, PITT, and EIS, J. Electrochem. Soc. 146 (1999) 1279. doi:10.1149/1.1391759.

[17]   X. Tang, C. Pan, L. He, L. Li, Z. Chen, A novel technique based on the ratio of potentio-charge capacity to galvano-charge capacity (RPG) for determination of the diffusion coefficient of intercalary species within insertion-host materials :

theories and experiments, Electrochim. Acta. 49 (2004) 3113–3119.
doi:10.1016/j.electacta.2004.02.025.

[18] W. Lehnert, W. Schmickler, The diffusion of lithium through graphite : a Monte
      Carlo simulation based on electronic structure, Chem. Phys. 163 (1992) 331–337.
      doi:https://doi.org/10.1016/0301-0104(92)87113-N.

[19] K. Persson, Y. Hinuma, Y. Meng, A. Van der Ven, G. Ceder, Thermodynamic and
      kinetic properties of the Li-graphite system from first-principles calculations, Phys.
      Rev. B. 82 (2010) 1–9. doi:10.1103/PhysRevB.82.125416.

[20] K. Persson, V.A. Sethuraman, L.J. Hardwick, Y. Hinuma, Y.S. Meng, A. Van Der Ven,
      V. Srinivasan, R. Kostecki, G. Ceder, Lithium Diffusion in Graphitic Carbon, J. Phys.
      Chem. Lett. 1 (2010) 1176–1180. doi:10.1021/jz100188d.

[21] R.N. Methekar, P.W.C. Northrop, K. Chen, R.D. Braatz, V.R. Subramanian, Kinetic
      Monte Carlo Simulation of Surface Heterogeneity in Graphite Anodes for Lithium-
      Ion Batteries: Passive Layer Formation, J. Electrochem. Soc. 158 (2011) A363.
      doi:10.1149/1.3548526.

[22] E.G. Leggesse, C. Chen, J. Jiang, Lithium diffusion in graphene and graphite : Effect
      of edge morphology, Carbon N. Y. 103 (2016) 209–216.
      doi:10.1016/j.carbon.2016.03.016.

[23] S. Krishnan, G. Brenet, E. Machado-charry, D. Caliste, L. Genovese, T. Deutsch, P.
      Pochet, Revisiting the domain model for lithium intercalated graphite, Appl. Phys.
      Lett. 103 (2014) 251904. doi:10.1063/1.4850877.

[24] R.B. Smith, E. Khoo, M.Z. Bazant, Intercalation Kinetics in Multiphase-Layered
      Materials, J. Phys. Chem. C. 121 (2017) 12505–12523.
      doi:10.1021/acs.jpcc.7b00185.

[25] M. Chandesris, D. Caliste, D. Jamet, P. Pochet, Thermodynamics and Related
      Kinetics of Staging in Intercalation Compounds, J. Phys. Chem. C. 123 (2019) 23711–
      23720. doi:10.1021/acs.jpcc.9b05298.

[26] Y. Chang, J. Jong, G.T. Fey, Kinetic Characterization of the Electrochemical Intercalation of Lithium Ions into Graphite Electrodes, J. Electrochem. Soc. 147 (2000) 2033–2038. doi:10.1149/1.1393481.

[27] S. Yang, H. Song, X. Chen, Electrochemical performance of expanded mesocarbon microbeads as anode material for lithium-ion batteries, Electrochem. Commun. 8 (2006) 137–142. doi:10.1016/j.elecom.2005.10.035.

[28] L. Pfaffmann, C. Birkenmaier, M. Müller, W. Bauer, F. Scheiba, T. Mitsch, J. Feinauer, Y. Kr, A. Hintennach, T. Schleid, V. Schmidt, H. Ehrenberg, Investigation of the electrochemically active surface area and lithium diffusion in graphite anodes by a novel OsO 4 staining method, J. Power Sources. 307 (2016) 762–771. doi:10.1016/j.jpowsour.2015.12.085.

[29] E.M. Perassi, E.P.M. Leiva, A theoretical model to determine intercalation entropy and enthalpy: Application to lithium/graphite, Electrochem. Commun. 65 (2016) 48–52. doi:10.1016/j.elecom.2016.02.003.

[30] E.M. Gavilán-Arriazu, O.A. Pinto, B.A.L. de Mishima, E.P.M. Leiva, O.A. Oviedo, Grand Canonical Monte Carlo Study of Li Intercalation into Graphite, J. Electrochem. Soc. 165 (2018) A2019–A2025. doi:10.1149/2.1211809jes.

[31] E.M. Gavilán-Arriazu, O.A. Pinto, B.A. López de Mishima, D.E. Barraco, O.A. Oviedo, E.P.M. Leiva, The kinetic origin of the Daumas-Hérold model for the Li-ion/graphite intercalation system, Electrochem. Commun. 93 (2018) 133–137. doi:10.1016/j.elecom.2018.07.004.

[32] N. Daumas, A. Hérold, Notes des Membres et Correspon- tants et Notes Présentéesou Transmises par Leurs Soins, C. R. Acad. Sci. Ser. C. 268 (1969) 373–375.

[33] K. a Fichthorn, W.H. Weinberg, Theoretical Foundations of Dynamic Monte-Carlo Simulations, J. Chem. Phys. 95 (1991) 1090–1096. doi:10.1063/1.461138.

[34] A.F. Voter, INTRODUCTION TO THE KINETIC MONTE CARLO METHOD, in: K.E.

Sickafus, E.A. Kotomin, B.P. Uberuaga (Eds.), Radiat. Eff. Solids, Springe, 2007: pp. 1–23. doi:10.1007/978-1-4020-5295-8_1.

[35]   P.A. Derosa, P.B. Balbuena, A Lattice-Gas Model Study of Lithium Intercalation in Graphite, J. Electrochem. Soc. 146 (1999) 3630. doi:10.1149/1.1392525.

[36]   E.M. Gavilán Arriazu, B.A. López De Mishima, O.A. Oviedo, E.P.M. Leiva, O.A. Pinto, Criticality of the phase transition on stage two in a lattice-gas model of a graphite anode in a lithium-ion battery, Phys. Chem. Chem. Phys. (2017). doi:10.1039/c7cp04253a.

[37]   F. Juarez, F. Dominguez-Flores, A. Goduljan, L. Mohammadzadeh, P. Quaino, E. Santos, W. Schmickler, Defying Coulomb's law: A lattice-induced attraction between lithium ions, Carbon N. Y. 139 (2018) 808–812. doi:10.1016/j.carbon.2018.07.039.

[38]   G. Brown, P.A. Rikvold, M.A. Novotny, A. Wieckowski, Simulated Dynamics of Underpotential Deposition of Cu with Sulfate on Au(111), J. Electrochem. Soc. 146 (1999) 1035–1040. doi:10.1149/1.1391717.

[39]   S.J. Mitchell, G. Brown, P.A. Rikvold, Dynamics of Br electrosorption on single-crystal Ag(100): A computational study, J. Electroanal. Chem. 493 (2000) 68–74. doi:10.1016/S0022-0728(00)00296-5.

[40]   N. Metropolis, A.W. Rosenbluth, M.N. Rosenbluth, A.H. Teller, E. Teller, Equation of state calculations by fast computing machines, J. Chem. Phys. 21 (1953) 1087–1092. doi:http://dx.doi.org/10.1063/1.1699114.

[41]   Y. Yamada, Y. Iriyama, T. Abe, Z. Ogumi, Kinetics of Lithium Ion Transfer at the Interface between Graphite and Liquid Electrolytes : Effects of Solvent and Surface Film, Langmuir. 25 (2009) 12766–12770. doi:10.1021/la901829v.

[42]   K. Xu, A. Von Cresce, U. Lee, Differentiating Contributions to " Ion Transfer " Barrier from Interphasial Resistance and Li þ Desolvation at Electrolyte / Graphite Interface, Langmuir. 26 (2010) 11538–11543. doi:10.1021/la1009994.

[43]   T. Abe, H. Fukuda, Y. Iriyama, Z. Ogumi, Solvated Li-Ion Transfer at Interface
        Between Graphite and Electrolyte, J. Electrochem. Soc. 151 (2004) 1120–1123.
        doi:10.1149/1.1763141.

[44]   K. Toyoura, Y. Koyama, A. Kuwabara, F. Oba, I. Tanaka, First-principles approach to
        chemical diffusion of lithium atoms in a graphite intercalation compound, Phys.
        Rev. B. 78 (2008) 1–12. doi:10.1103/PhysRevB.78.214303.

[45]   A.J. Bard, L.R. Faulkner, Electrochemical Methods : Fundamentals and Applications,
        2001.

[46]   B. Tao, L.C. Yule, E. Daviddi, C.L. Bentley, P.R. Unwin, Correlative Electrochemical
        Microscopy of Li-Ion (De)intercalation at a Series of Individual LiMn2O4 Particles,
        Angew. Chemie - Int. Ed. 58 (2019) 4606–4611. doi:10.1002/anie.201814505.

[47]   M. Inaba, H. Yoshida, Z. Ogumi, T. Abe, Y. Mitzutani, M. Asano, In Situ Raman Study
        on Electrochemical Li Intercalation into Graphite, J. Electrochem. Soc. 142 (1995)
        20. doi:10.1149/1.2043869.

[48]   C. Uebing, R. Gomer, A Monte Carlo study of surface diffusion coefficients in the
        presence of adsorbate–adsorbate interactions. I. Repulsive interactions, J. Chem.
        Phys. 95 (1991) 7626–7635. doi:10.1063/1.461336.

[49]   R. Kobayashi, N. Ohba, T. Tamura, S. Ogata, A Monte Carlo Study of Host-Material
        Deformation Effect on Li Migration in Graphite, J. Phys. Soc. Japan. 82 (2013) 1–8.

[50]   E.P.M. Leiva, E. Perassi, D. Barraco, Shedding Light on the Entropy Change Found for
        the Transition Stage II→Stage I of Li-Ion Storage in Graphite, J. Electrochem. Soc.
        164 (2017) A6154–A6157. doi:10.1149/2.0231701jes.

[51]   M. Otero, A. Sigal, E.M. Perassi, D. Barraco, E.P.M. Leiva, Statistical mechanical
        modeling of the transition Stage II → Stage I of Li-ion storage in graphite. A priori vs
        induced heterogeneity, Electrochim. Acta. 245 (2017) 569–574.
        doi:10.1016/j.electacta.2017.05.128.

[52]   M.P. Mercer, S. Finnigan, D. Kramer, D. Richards, H.E. Hoster, The influence of point defects on the entropy profiles of Lithium Ion Battery cathodes: a lattice-gas Monte Carlo study, Electrochim. Acta. 241 (2017) 141–152. doi:10.1016/j.electacta.2017.04.115.

[53]   D.W. Dees, K.G. Gallagher, D.P. Abraham, A.N. Jansen, Electrochemical Modeling the Impedance of a Lithium-Ion Positive Electrode Single Particle, J. Electrochem. Soc. 160 (2013) 478–486. doi:10.1149/2.055303jes.

[54]   M. Ecker, T.K.D. Tran, P. Dechent, S. Käbitz, A. Warnecke, D.U. Sauera, Parameterization of a physico-chemical model of a lithium-ion battery: I. Determination of parameters, J. Electrochem. Soc. 162 (2015) A1836–A1848. doi:10.1149/2.0551509jes.

[55]   W. Rüdorff, U. Hofmann, Über Graphitsaelze, Zeitshrift Fur Anorg. Und Allg. Chemie. 238 (1938) 1–50. doi:10.1002/zaac.19382380102.

[56]   M.P. Mercer, M. Otero, M. Ferrer-Huerta, A. Sigal, D.E. Barraco, H.E. Hoster, E.P.M. Leiva, Transitions of lithium occupation in graphite: A physically informed model in the dilute lithium occupation limit supported by electrochemical and thermodynamic measurements, Electrochim. Acta. 324 (2019) 134774. doi:10.1016/j.electacta.2019.134774.
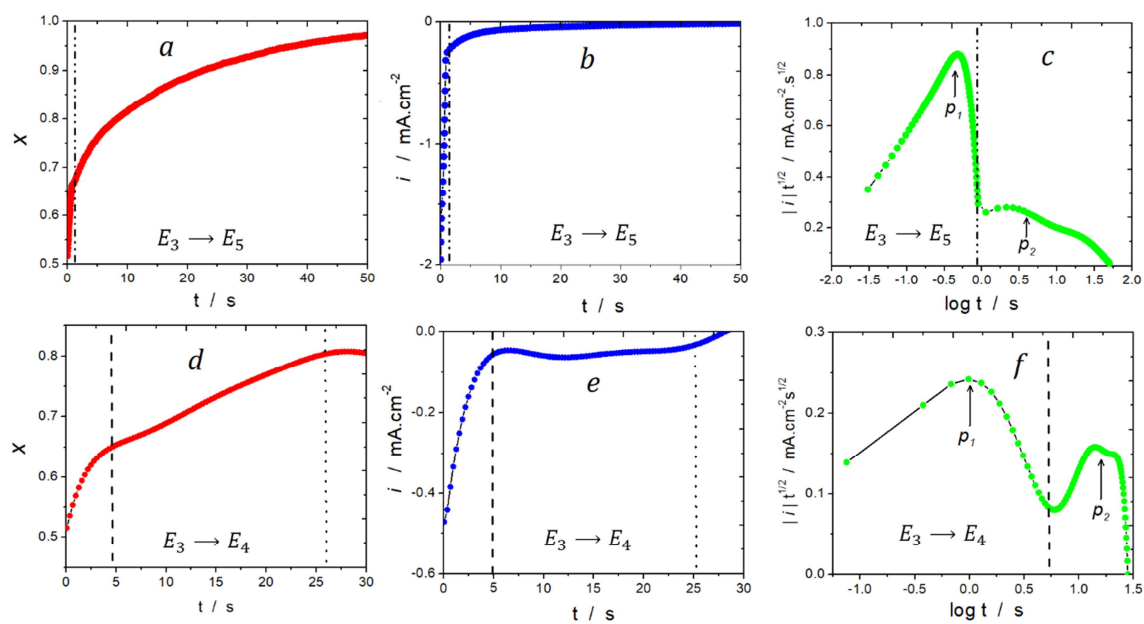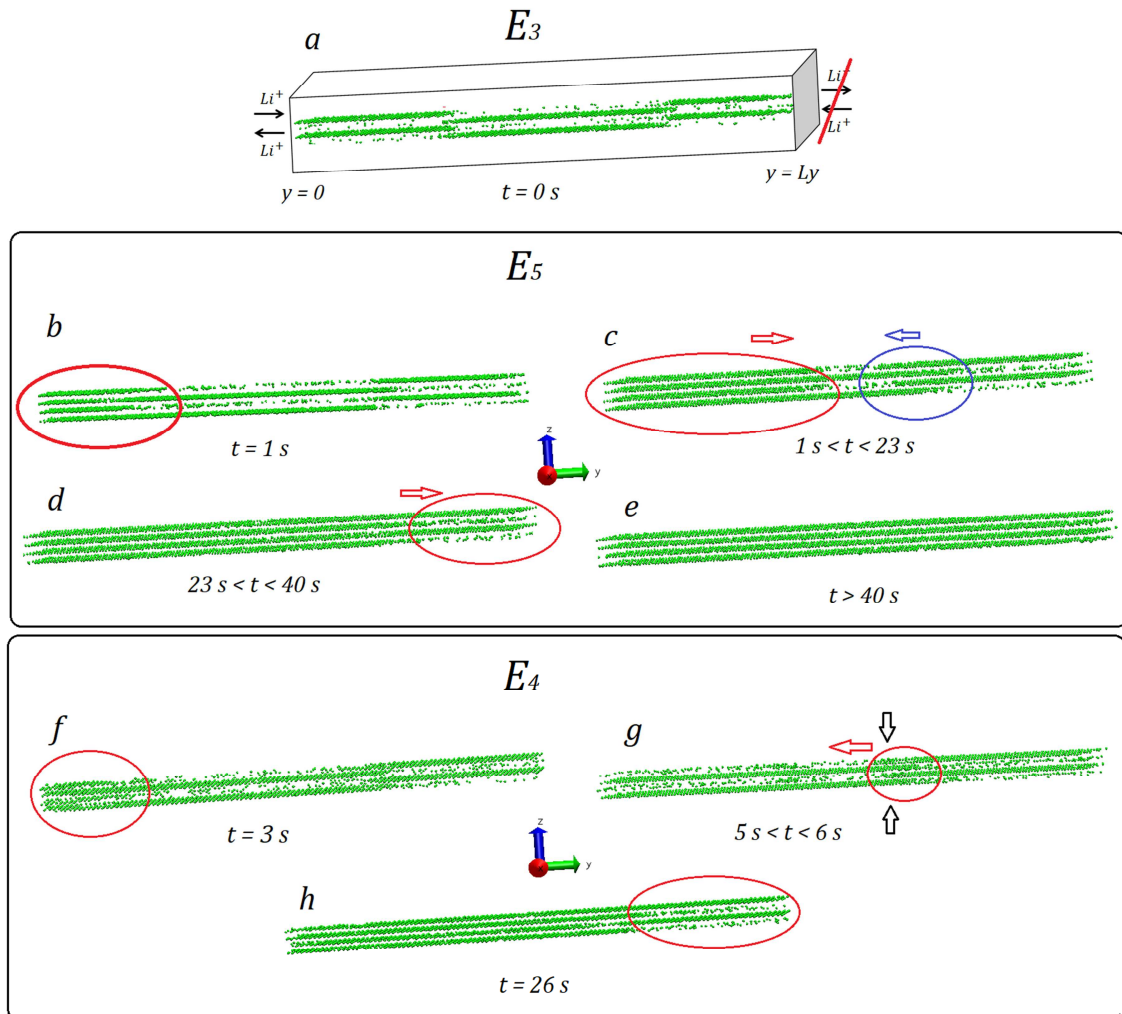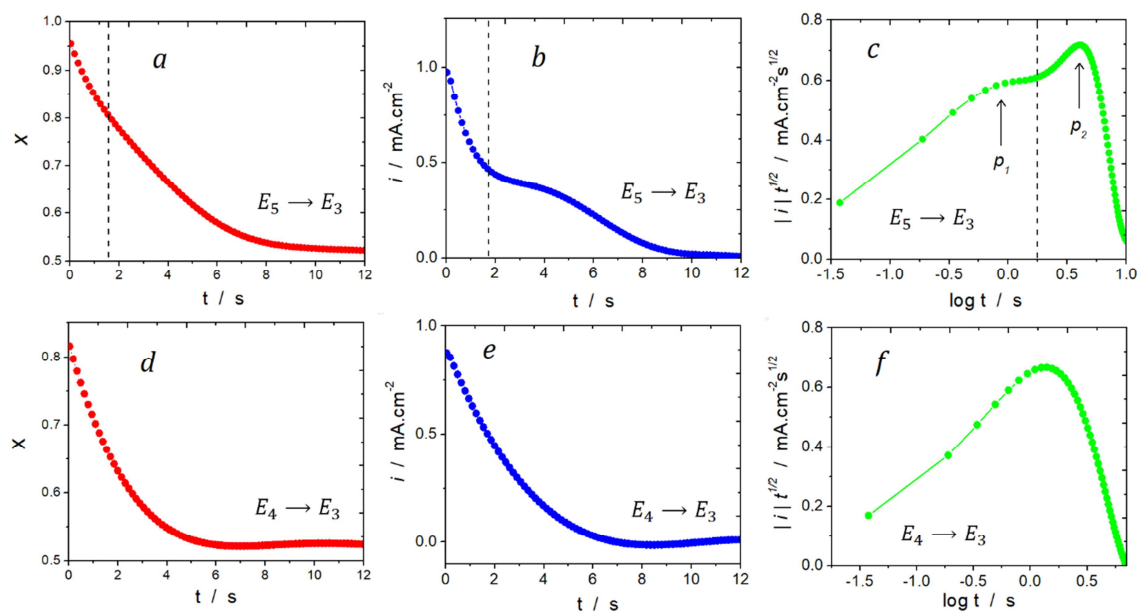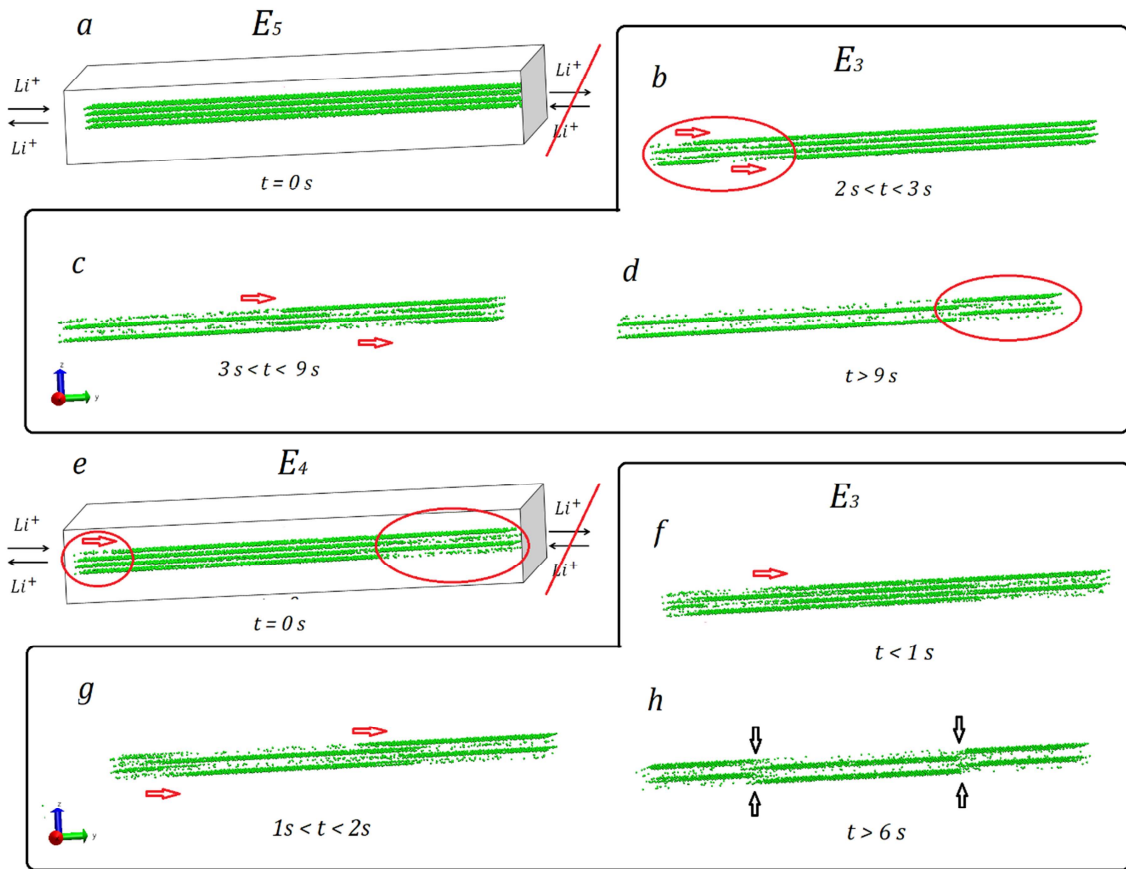
Figure 1:
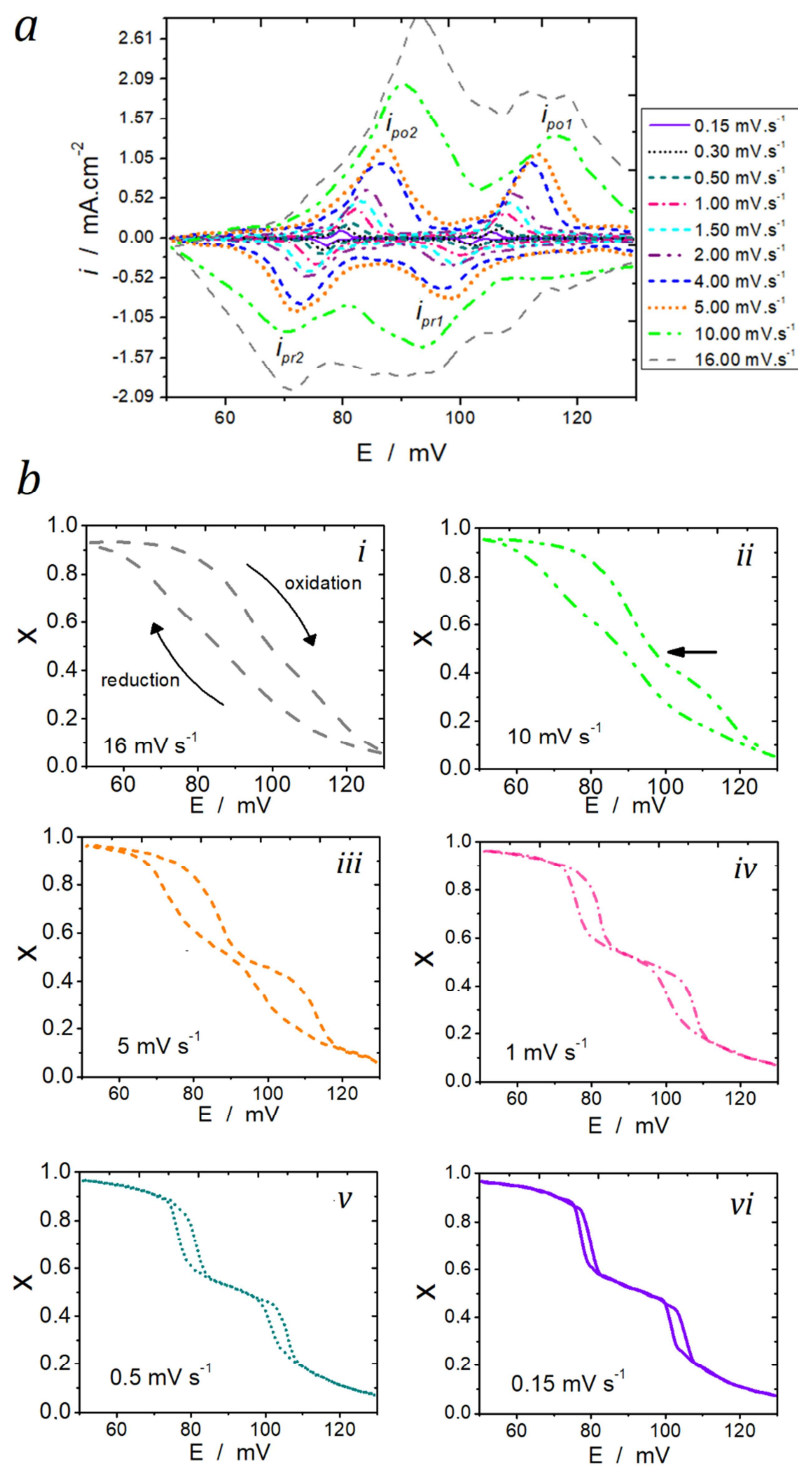
Figure 2:
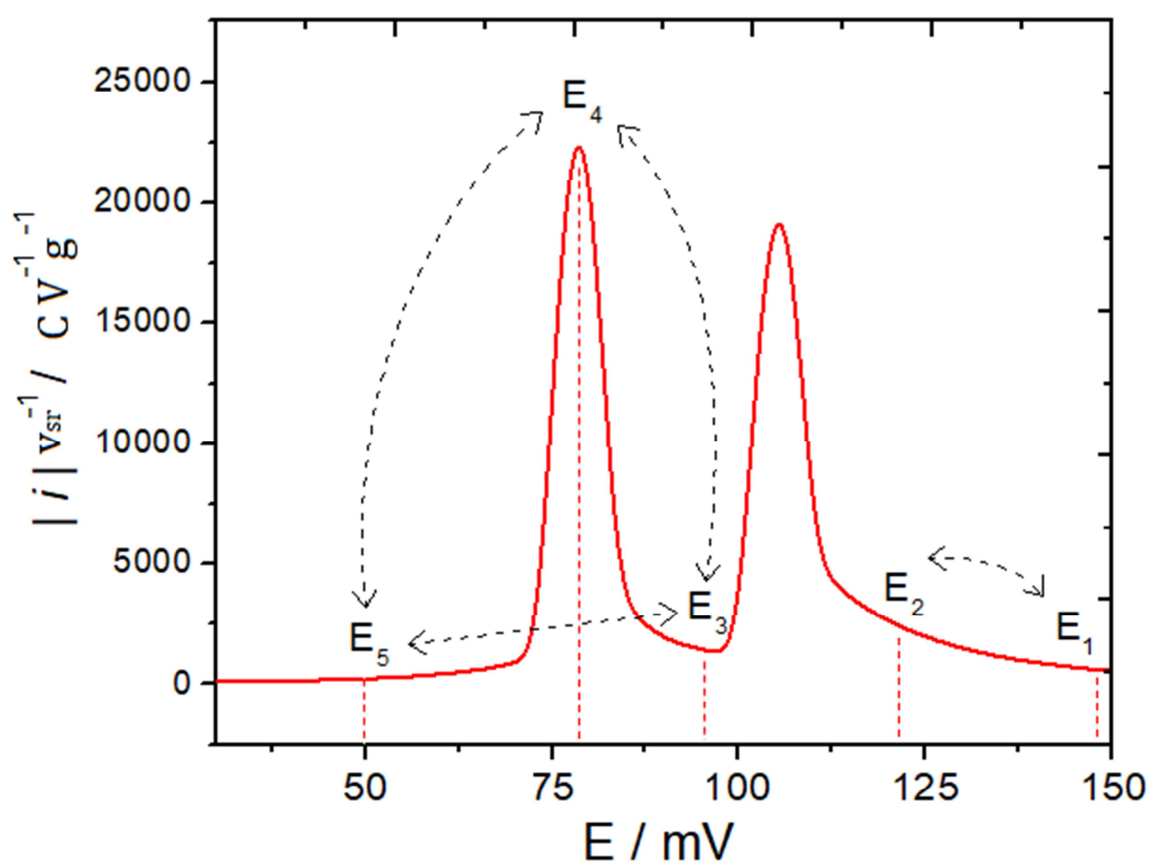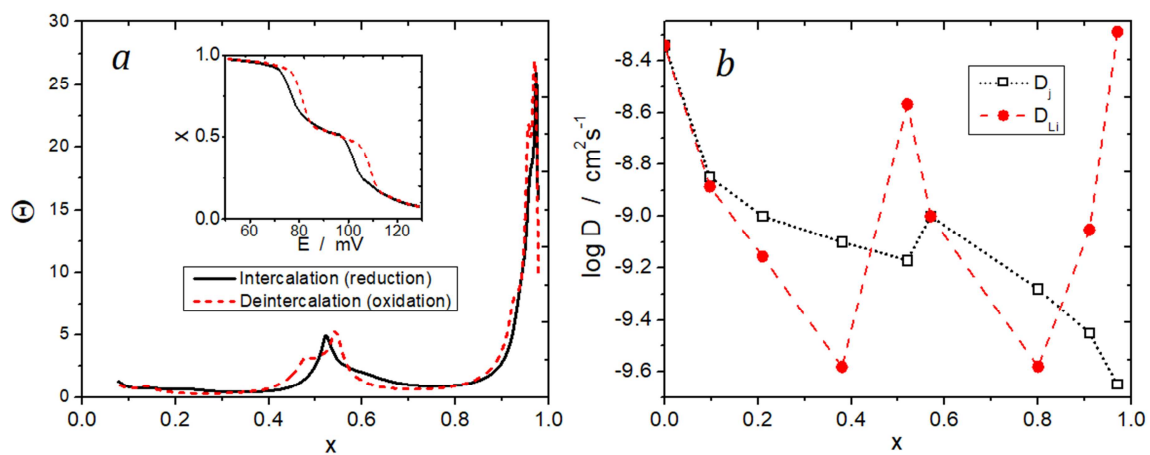
Figure 3:
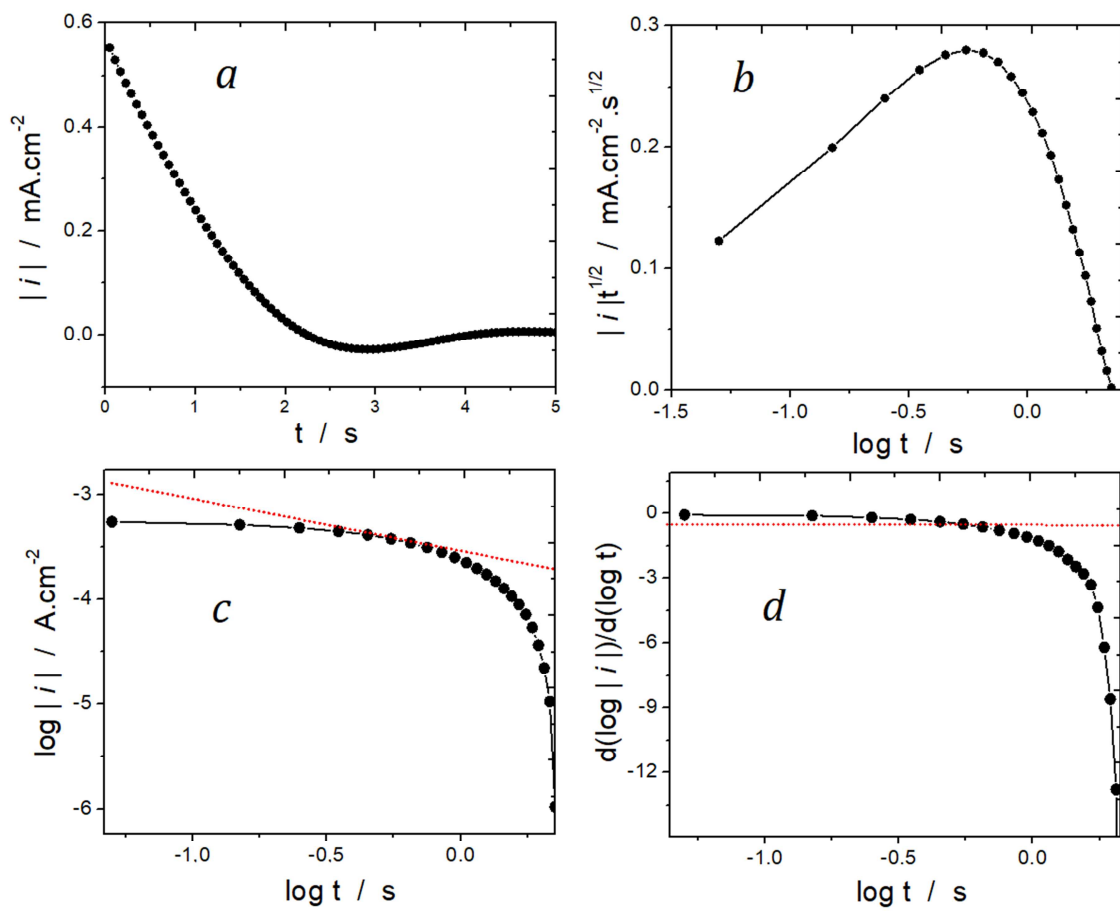
Figure 4:

Figure 5:
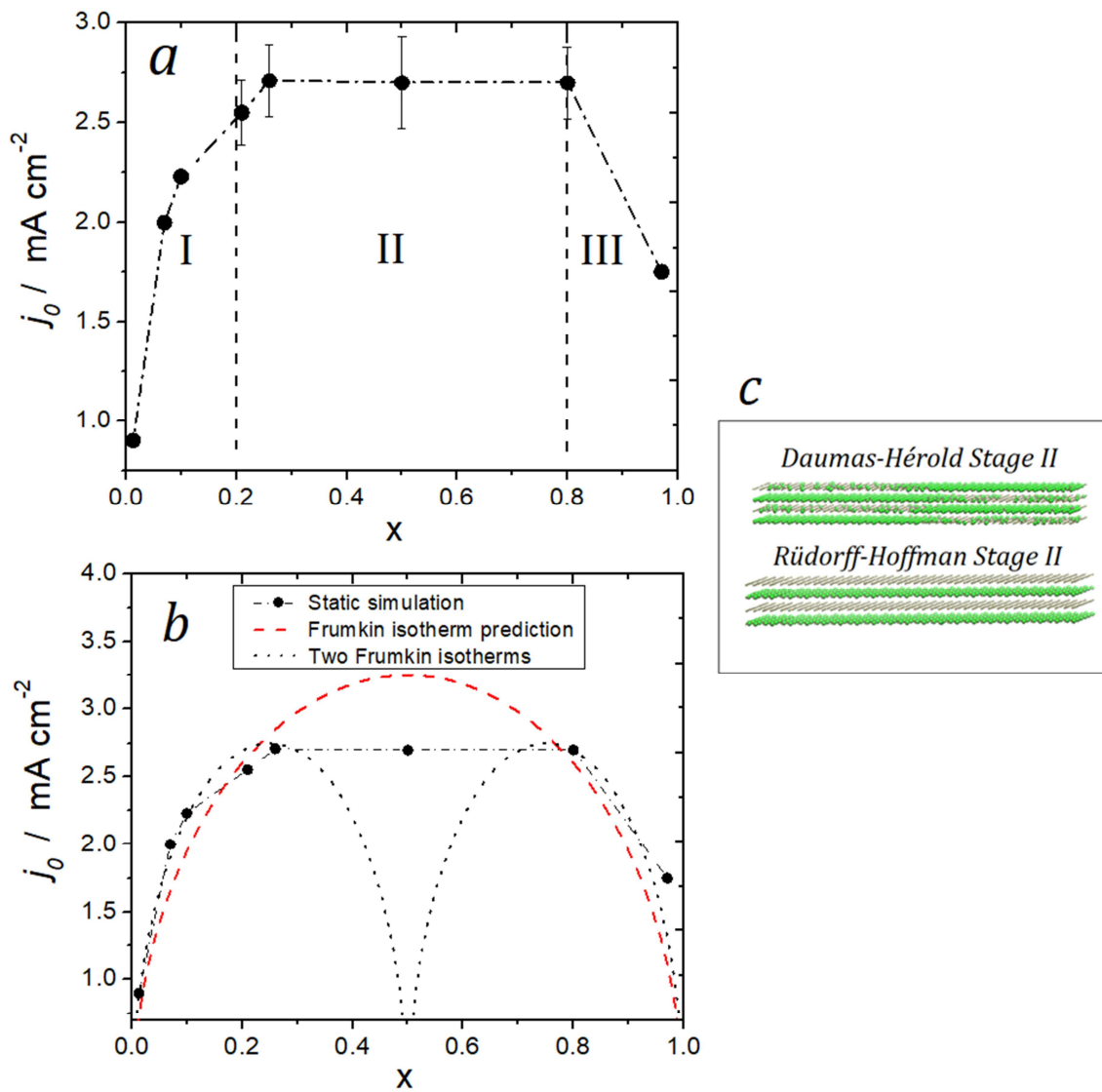
Figure 6:

Figure 7:

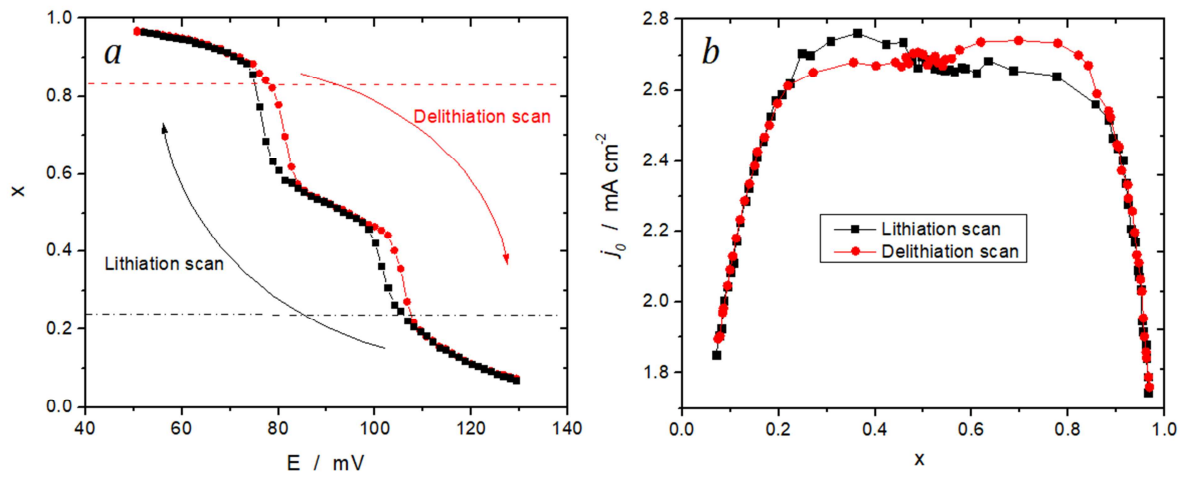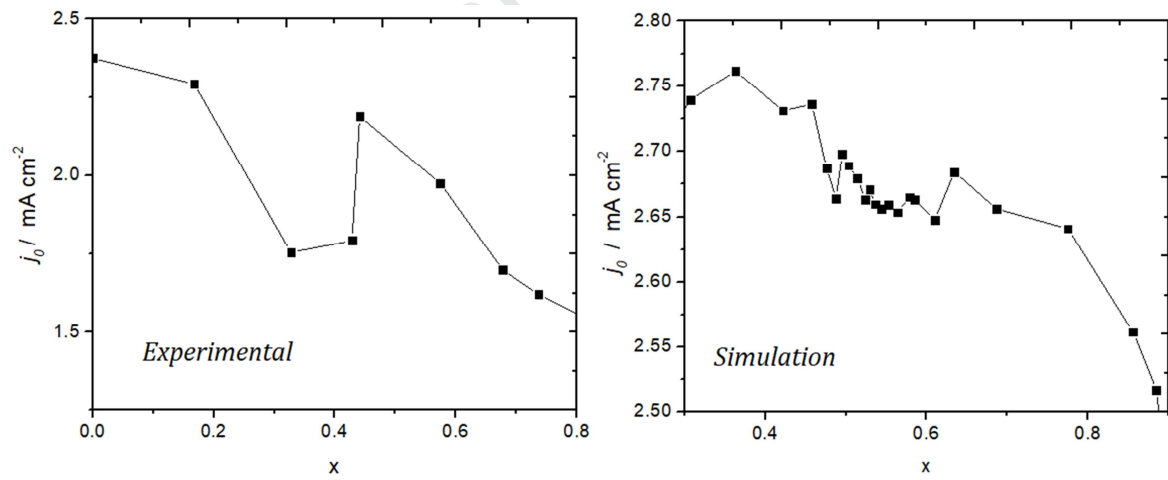Figure 8:

Figure 9:

Figure 10:

Figure 11:

Highlights:

- Kinetic Monte Carlo simulations emulate electrochemical techniques allowing a deep atomistic study.
- Cyclic voltammetry and chronoamperometric simulations profiles provide understanding on experimental results.
- Diffusion coefficients and exchange current density predict the behavior of Li-ion in different intercalation levels.
- Deintercalation is faster than intercalation, due to the Li-ion clog next to the interphase in the lithiation.
- The hysteresis phenomenon is apparently related to a kinetic origin.

Declaration of interests

☒ The authors declare that they have no known competing financial interests or personal relationships that could have appeared to influence the work reported in this paper.

☐The authors declare the following financial interests/personal relationships which may be considered as potential competing interests: